Effect of folds and pockets on the topology and propagation of premixed turbulent flames

N. Fogla[a*], F. Creta[b], M. Matalon[a]

[a]*University of Illinois at Urbana-Champaign, Urbana, IL 61801, USA*

[b]*University of Rome "La Sapienza", Rome, Italy*

Abstract

Propagation of premixed turbulent flames is examined using a hybrid Navier–Stokes/front tracking methodology, within the context of a hydrodynamic model. The flame, treated as a surface of density discontinuity separating the burned and unburned gases, propagates relative to the fresh mixture at a speed that depends on the local mixture (through a Markstein length) and flow conditions (through the stretch rate), and the flow field is modified in turn by gas expansion; only positive Markstein length are considered, where thermo-diffusive instabilities are absent. Depending on the Markstein length, we have identified in a previous publication two modes of propagation - *sub-critical* and *super-critical*, based on whether the effects of the Darrieus-Landau instability are absent or dominant, respectively. The results were limited to low turbulence intensities where the mathematical representation of the flame front was based on an explicit single-valued function. In the present paper we utilize a generalized representation of the flame surface that allows for multivalued and disjointed interfaces, thus extending the results to higher turbulence intensities. We show that when increasing the turbulence intensity the influence of the Darrieus-Landau instability on the super-critical mode of propagation progressively decreases and in the newly identified *highly-turbulent regime* the flame is dominated completely by the turbulence for all values of Markstein numbers; i.e., with no distinction between sub- and super-critical conditions. Primary importance is given to the determination of the turbulent flame speed and its dependence on turbulence intensity which, when increasing the turbulence level, transitions from a quadratic to a sub-linear scaling. Moreover, the exponent of the sub-linear scaling for the turbulent flame speed is generally lower than the corresponding exponent for the scaling of the flame surface area ratio, which is often used for experimentally determining the turbulent flame speed. We show that the leveling in the rate of increase of the turbulent flame speed with turbulence intensity, is due to frequent flame folding and detachment of pockets of unburned gas that cause a reduction in the average main surface area of the flame, while the lower exponents in the scaling law for the turbulent flame speed compared to that of the flame surface area ratio is due to flame stretching. Disregarding the effect of flame stretch for mixtures of positive Markstein length results in overestimating the turbulent flame speed. Finally, we characterize the flame turbulence interaction via quantities such as the mean vorticity and mean strain, illustrating the effects of incoming turbulence on the flame and the modification of the flow by the flame on the unburned and burned sides.

Keywords: premixed flames, turbulent flame speed, Darrieus-Landau instability, folds and pockets, flame stretch

1. Introduction

One of the most important quantities characterizing premixed turbulent combustion is the *turbulent flame speed* defined as the mean propagation speed of a premixed flame into a (homogeneous) turbulent gaseous mixture of zero mean velocity, similar to the *laminar flame speed* defined as the propagation speed of a (planar and adiabatic) premixed flame into a quiescent mixture. Knowledge of the turbulent flame speed allows predicting the average rate of energy release, or equivalently the mean rate of fuel consumption in a combustor, which controls important design considerations of automotive engines, industrial gas turbines and industrial furnaces, and is also relevant to fire safety concerns and astrophysical

---

*Corresponding author

Email addresses: `fogla1@illinois.edu` (N. Fogla[a*]), `francesco.creta@uniroma1.it` (F. Creta[b]), `matalon@illinois.edu` (M. Matalon[a])

problems, such as explosion in type Ia supernovae.

The determination of the turbulent flame speed has been a subject of intensive theoretical, computational and experimental studies. The experimental data collected more than two decades ago by Abdel-Gayed et al. [1] from a large number of studies (approximately 1650 experiments), and the more recent compilation by Lipatnikov and Chomiak [2] show a wide quantitative scatter in the measured values obtained by different investigators. This has been partially attributed to the different experimental configurations used, particularly flame geometry and initial conditions, and to the prevalent flow conditions [3]. Nevertheless, some common features have been observed; first, being the increase in speed with increasing turbulence intensity attributed to the increase in flame surface area, and second, the relatively small increase in speed beyond a certain turbulence level, commonly referred to as the *bending effect*.

In attempting to analyze the experimental data, theoretical studies have primarily adopted Damköhler's hypothesis [4] that the ratio of the turbulent flame speed S_T to the laminar flame speed S_L is equal to the increase in surface area of the wrinkled flame, such that $S_T/S_L = A_T/A$ where A_T and A are, respectively, the surface areas of the turbulent and (planar) laminar flames. Resorting to geometrical arguments with analogy to a Bunsen flame, Damköhler further deduced that the area ratio for large-scale turbulence is proportional to v'_c/S_L, where v'_c is the turbulence intensity (i.e., the r.m.s. of velocity fluctuations). Extending this phenomenology, Shelkin [5] argued that Damköhler's proposition is only valid for high-intensity turbulence ($v'_c \gg S_L$) and that a quadratic law of the form

$$S_T/S_L = 1 + \tfrac{1}{2}(v'_c/S_L)^2 \qquad (1)$$

results for low-intensity turbulence ($v'_c \ll S_L$). A more rigorous approach undertaken by Clavin and Williams [6] using a multiscale perturbative method led also to a quadratic law, similar to the heuristic result (1) but without the factor $1/2$. For dynamically passive interfaces propagating in weak-turbulence (considered as white noise) at a constant speed it was shown [7, 8] that the quadratic dependence on turbulence intensity is only transient, and that the long-time behavior tends to a slightly smaller speed $\sim v_c'^{4/3}$. In the absence of a sound theory, expressions of the form

$$S_T/S_L = 1 + C\left(v'_c/S_L\right)^n \qquad (2)$$

with empirical constants C and adjustment exponents

n were proposed by various investigators using scaling and physical arguments, efficiency functions and renormalization techniques [9–16], or based on experimental data [17–22].

A related issue concerns the role of the hydrodynamic, or Darrieus-Landau (DL) instability [23, 24] on the turbulent flame and its propagation speed. A number of experimental studies have addressed this issue [19, 22, 25–28], concluding that the influence of the DL instability is limited to low-to-moderate turbulence intensities. Assuming the effects of turbulence and DL instability are additive, Akkerman and Bychkov [29] used a model equation for the evolution of the flame front to show that the instability leads to enhancement in the turbulent flame speed. An estimate of the range of DL influence was presented in [30] by comparing the growth rate of the instability to a characteristic eddy frequency. Conditions for the DL enhancement in terms of turbulent intensity and turbulent-to-laminar flame length ratio were also obtained from the simulations of Boughanem and Trouvé [31].

In recent years, Direct Numerical Simulations (DNS) have been used more frequently to study the interaction of turbulence with flames. However, the high computational cost involved limits the scope of such studies by restricting the investigation to small domains and short time intervals, and focusing on a particular set of conditions associated with a specific mixture. With the exception of Bell et al. [32] who carried out three-dimensional calculations with a detailed chemical mechanism (with a mixture model for diffusion), most studies have either adopted a one-step or reduced mechanism for the chemistry [33–35] or performed the simulations in two-dimensions [36–38]. Only few of these studies commented directly on the turbulent flame speed and its dependence on the turbulence and combustion characteristics. At the present DNS is not an accessible tool that permits a comprehensive investigation of the propagation of turbulent flames while spanning the large set of relevant parameters. Numerical methods that require modest computational resources, such as Reynolds Averaged Navier–Stokes (RANS) or Large Eddy Simulation (LES), depend heavily on the adopted closure assumptions or sub-grid model used, making the accuracy of these results difficult to assess.

The present work will address the complex dynamics that result from flame interaction with turbulence in the context of the asymptotic hydrodynamic theory, systematically *derived* using a multi-scale approach that exploits the disparity between the diffusion length representing the flame thickness and the characteristic hydrodynamic length scale [39, 40]. The flame, represented as a sur-

face separating burned from unburned gases with different densities and temperatures, propagates relative to the fresh mixture at a speed that depends on the local stretch rate, modulated by a coefficient known as the Markstein length that mimics the influences of diffusion and chemical reaction occurring inside the flame zone. The propagation is therefore affected by the local mixture composition, through the Markstein length, and by the flow conditions, through the flame stretch consisting of the curvature of the flame surface and the underlying hydrodynamic strain it experiences. The flow field is modified in turn by the gas expansion resulting from the increase in temperature caused by the heat release. The formulation, which is valid for flame propagation in laminar or turbulent flows, is based on physical first principles, free of modeling assumptions and/or ad-hoc parameters commonly used in turbulence studies.

In the hydrodynamic model the location of the flame surface is unambiguously identified and, as a result, quantities related to the flame surface, such as speed, curvature and flame stretch, are easily and *uniquely* determined. This marks a clear advantage over DNS, where one is faced with the difficulty of selecting an appropriate iso-surface of temperature or concentration to represent the flame surface. A poor choice of the isosurface could lead to uncertainties in the flame displacement speed [41], and different contours could lead to significantly different values of turbulent flame speed [35]. Another advantage of our methodology is the ability, through a closed-loop flow control system, to regulate the mean flame position and the turbulent intensity immediately ahead of the flame. This permits reporting on the dependence of the propagation speed on the turbulence intensity experienced by the flame, rather than the turbulence level at the inflow boundary where it has been introduced. Finally, our model, which intends primarily to elucidate on the intricate flame-turbulence interactions, is a natural extension of the rigorous perturbative studies into the nonlinear regime, while relaxing the assumptions of negligible thermal expansion, weak velocity fluctuations or small flame displacements.

Implicit in the hydrodynamic description is the assumption that the small turbulent eddies do not modify the chemistry and transport inside the flame, which retains its laminar structure with transport and chemistry accounted for through the Markstein length. Strictly speaking, therefore, the results fall in the "large scale regime" of turbulent combustion based on Damköhler's classification, or in the "flamelet regime" based on the refined combustion regime diagrams proposed in recent years [42, 43]. It

should be recognized, however, that the regime diagrams provide only a *qualitative classification* of the possible flame-turbulence interactions, obtained by comparing various turbulent time scales with their laminar counterparts. The flamelet regime in this description is characterized by a sufficiently small Karlovitz number Ka, representing the ratio of the residence time within the flame to the Kolmogorov turnover time. In the regime corresponding to $Ka > 1$, referred to as the "distributed reaction zone" regime, the residence time is larger than the Kolmogorov time scale implying that small scale eddies do penetrate the flame zone and therefore could possibly modify its internal structure. However, there is no evidence to-date neither from experiments nor from simulations, that turbulent transport leads necessarily to broadening of the flame preheat and reaction zones. For example, Shepherd et al. [44] observed lean methane-air flamelets with $Ka \sim 1$ - 17, and found that even at the highest Karlovitz numbers the internal flamelet structures remained unaffected by the turbulence and were similar to those derived from laminar flame calculations. Similarly, the piloted premixed flames in the experiment of Dunn et al. [45] corresponding to $Ka \sim 100$ - 3500 did no show evidence of flame broadening, even when reducing the Damköhler number to sufficiently low values. Numerous other examples were given by Driscoll [3, Table 2] who states that "*the criterion that flamelets become thick when Karlovitz number exceeds unity does not appear to be realistic.*" In a recent DNS study Poludnenko and Oran [34, 35] point out that although the preheat zone does show evidence of broadening, " *this effect, while statistically significant, is fairly small with the width of the preheat zone increasing by less than a factor of two.*" They conclude that "*the turbulent cascade fails to penetrate the internal flame structure, and thus the action of small-scale turbulence is suppressed throughout most of the flame*". Thus, although the hydrodynamic model does not allow the broadening of the preheat zone, it is possible, that the results of this model extend beyond the flamelet regime, and must therefore be judged by comparison to the experimental record.

In our earlier work [46], where the first application of the hydrodynamic model to turbulent flames was presented, we have identified two modes of propagation that were termed sub- and super-critical, in analogy with the bifurcation property of a laminar flame that results from the DL instability. Under laminar conditions, a planar flame transitions beyond criticality to a stable large-scale conformation with a sharp peak protruding into the burned gas that propagates steadily at a speed $U_L > S_L$. Similarly, in the sub-critical regime the turbulent flame is not

affected by the DL instability and remains statistically planar, i.e., with zero mean curvature. In the super-critical regime the turbulent flame is strongly affected by the instability and develops frequent sharp crests pointing towards the burned gas, which is the hallmark of the DL instability. Moreover, this highly-corrugated flame exhibits resiliency to the turbulence, retaining its distinct shape during the fluctuations at least at low turbulence levels. The flame propagation speed in these two regimes also differs substantially. Although in both cases the increase in speed varies quadratically with turbulence intensity, the highly-corrugated flame in the super-critical regime propagates at a higher speed than the nearly-planar flame in the sub-critical regime does, because of its larger surface area. These earlier results were limited to low turbulence intensities. The limitation was due to the restrictive mathematical representation of the flame surface as a single valued function. In the current work we utilize a generalized representation which allows for multivalued and disjointed interfaces, thus extending our results to higher turbulence intensities where the development of folds and creation of pockets are ubiquitous. Our objective is to systematically understand the effects of such highly convoluted flame topologies on the flame propagation. A related question pertains to the influence of the DL instability, whether it remains a significant factor in affecting the flame propagation as it did at low turbulent intensities.

For simplicity, the computations presented below are limited to flame propagation in a "two-dimensional turbulent flow". We have also limited the discussion to mixtures with positive values of Markstein length, such as lean hydrocarbon- or rich hydrogen-air mixtures, that are not contaminated by thermo-diffusive instabilities. Despite the adopted idealization our results correlate well with experimental data, provide unique insight into the morphology, including flame folding and detachment, of turbulent flames, and clarify the role of the DL instability on their propagation. We show that the distinction between sub- and super-critical regimes, namely where influences of the DL instability are absent or dominant, is limited to low turbulence intensities and that these differences progressively decrease at sufficiently high values of the turbulence intensity where a "highly-turbulent regime" evolves with the flame controlled primarily by the turbulence. The various regimes are clearly delineated by statistical properties of various flame characteristics, including the thickness of the flame brush, flame curvature and hydrodynamic strain. Another novelty of this work is the extraction of scaling laws for the turbulent flame speed S_T and its dependence on turbulence intensity, in

each of these regimes. We find that the dependence of S_T on turbulence intensity varies from a quadratic law at low intensities, associated primarily to the increase in flame surface area, to a sub-linear law that results from the decrease in speed stemming from flame folding and frequent detachment of unburned gas pockets, and from the drop in the mean local flame speed due to flame stretching.

2. Formulation

Deflagrative combustion processes are highly subsonic and a quasi-isobaric limit approximation may be employed for their description. Accordingly, the system pressure is nearly constant, and the gradient of the small pressure variations (on the order of the representative Mach number squared) balance the correspondingly small momentum changes. The hydrodynamic equations, consisting of mass and momentum conservation, are

$$\frac{D\rho}{Dt} + \rho\nabla\cdot\mathbf{v} = 0 \tag{3}$$

$$\rho\frac{D\mathbf{v}}{Dt} = -\nabla p + \nabla\cdot\mu\,\mathbf{\Sigma} \tag{4}$$

where ρ, μ are the density and viscosity of the mixture, $\mathbf{v}$ the gas velocity, p the pressure, and

$$\mathbf{\Sigma} = 2\mathbf{E} - \tfrac{2}{3}(\nabla\cdot\mathbf{v})\mathbf{I}, \quad \mathbf{E} = \tfrac{1}{2}\big(\nabla\mathbf{v} + (\nabla\mathbf{v})^{\mathrm{T}}\big)$$

the viscous stress and strain rate tensors, respectively, with $\mathbf{I}$ the unit tensor (the superscript T denotes the transpose). These equations must be supplemented by an energy equation for the entire mixture and mass balance equations for the fuel (denoted by F) and oxidizer (denoted by O), which take the form

$$\rho c_p \frac{DT}{Dt} - \nabla\cdot\lambda\nabla T = Q\,\varpi \tag{5}$$

$$\rho\frac{DY_i}{Dt} - \nabla\cdot\rho\mathcal{D}_i\nabla Y_i = -\nu_i W_i\,\varpi, \quad i = F, O \tag{6}$$

where T is the temperature, λ, c_p the thermal conductivity and specific heat of the mixture, Y_i, ν_i, W_i and $\mathcal{D}_i$ the mass fraction, stoichiometric coefficient, molecular weight and molecular diffusivity of species i, and Q the total heat release. The chemical activity between the fuel and oxidizer is modeled by a one-step overall reaction that proceeds at a rate

$$\varpi = \mathcal{B}\,\rho^2\,Y_F^a Y_O^b\,e^{-E/\mathcal{R}T} \tag{7}$$

with a, b the reaction orders, E the activation energy, $\mathcal{R}$ the gas constant and $\mathcal{B}$ an appropriately defined pre-

exponential factor. The equation of state is

$$\rho T = (W/\mathcal{R})P_0 \qquad (8)$$

where W is the mixture molecular weight (assumed constant). The transport coefficients $\mu, \lambda/c_p, \rho\mathcal{D}_i$ are assumed to have the same temperature dependence, implying that their ratio is constant; in particular

$$\lambda/\rho c_p \mathcal{D}_F = Le_F, \qquad \lambda/\rho c_p \mathcal{D}_O = Le_O$$

are the Lewis numbers of the fuel and oxidizer, respectively.

2.1. The hydrodynamic model

The hydrodynamic theory exploits the disparity of the diffusion length scale $l_f = \lambda_u/\rho_u c_p S_L$, which characterizes the flame zone, and the hydrodynamic length scale L that represents the domain within which the flame propagates; the subscript u identifies the state of the unburned gas. When $\delta \equiv l_f/L \ll 1$, the entire flame consisting of the preheat and reaction zones is a thin layer embedded in the flow field which, when viewed on the hydrodynamical scale, can be treated as a surface. This surface can be determined by $\psi(\mathbf{x}, t) = 0$, where ψ is a smooth scalar function with $\psi < 0$ on the unburned and $\psi > 0$ on the burned regions. The flame separates the fresh mixture with temperature T_u and density ρ_u from the burned products with temperature T_b and density ρ_b, and propagates relative to the unburned gas at a speed

$$S_f \equiv -V_f + \mathbf{v}^* \cdot \mathbf{n} \qquad (9)$$

where V_f is the absolute speed at which a point on the flame surface moves relative to a fixed coordinate system, $\mathbf{n}$ is a unit normal to the surface pointing towards the burned gas, and $\mathbf{v}$ is the gas velocity with the $*$ indicating that is has been evaluated on the unburned side of the flame front. The flame speed is determined by integrating the energy and species equations (5)-(6) across the flame. For thin flames the integration is, to leading order, carried along the normal to the flame surface with effects due to its finite thickness that include accumulation and transverse fluxes accounted for as $O(\delta)$ corrections. The result is an expression for the flame speed,

$$S_f = S_L - \mathscr{L}\,\mathbb{K}, \qquad (10)$$

where $\mathbb{K} = S_L\kappa + K_S$ is the flame stretch rate, which incorporates the effects of curvature $\kappa = -\nabla \cdot \mathbf{n}$ and hydrodynamic strain $K_S = -\mathbf{n} \cdot \mathbf{E} \cdot \mathbf{n}$. The parameter $\mathscr{L}$ known as the Markstein length is proportional to the flame

thickness l_f and depends on the effective Lewis number of the mixture (an average of the individual Lewis numbers Le_F and Le_O, weighted more heavily with respect to the deficient component in the mixture), the functional dependence of the transport coefficients on temperature, the thermal expansion parameter $\sigma \equiv \rho_u/\rho_b = T_b/T_u$, and the Zel'dovich number or activation energy parameter. Using the expressions for $\mathbf{n} = \nabla\psi/|\nabla\psi|$ and $V_f = -\psi_t/|\nabla\psi|$, the flame speed definition (9) can be cast in the form of an evolution equation

$$\psi_t + \mathbf{v}^* \cdot \nabla\psi = S_f|\nabla\psi|, \qquad (11)$$

that describes the instantaneous shape and location of the flame surface, with S_f given by (10). Further details can be found in [39, 40].

The flow on either side of the flame sheet is governed by the Navier–Stokes (NS) equations (3)-(4), with

$$\rho = \begin{cases} \rho_u & \text{for } \psi(\mathbf{x},t) < 0 \\ \rho_b & \text{for } \psi(\mathbf{x},t) > 0, \end{cases} \qquad (12)$$

A similar representation to (12) can be adopted for the viscosity μ but in the present study it will be assumed constant. Conservation of mass and momentum across the flame surface is enforced through the Rankine-Hugoniot jump relations. It is convenient for numerical integration to adopt a *continuum* approach by smoothing the piecewise constant density via a *tanh*-like function over a small distance h, centered at $\psi(\mathbf{x}, t) = 0$. The numerical thickness h is independent of the flame thickness δ and must be chosen as small as possible. The NS equations then reduce to

$$\nabla \cdot \mathbf{v} = \rho_u S_f \frac{\partial}{\partial n}\left(\frac{1}{\rho}\right) \qquad (13a)$$

$$\rho \frac{D\mathbf{v}}{Dt} = -\nabla\hat{p} + \mu\nabla^2\mathbf{v}, \qquad (13b)$$

where the source term on the right hand side of (13a) represents the gas expansion, and

$$\hat{p} = p - \tfrac{1}{3}\mu(\nabla \cdot \mathbf{v})$$

is the reduced pressure. The viscous term in (13b) is of $O(\delta)$ and must be treated small, for consistency, by properly choosing the viscosity μ. These equations are solved along with the evolution equation (11) for the determination of $\psi(\mathbf{x}, t)$, with the flame represented by its zero level set. It is easily verified by integrating Eqs. (13a)-(13b) across the flame surface and taking the limit $h \to 0$, that the Rankine-Hugoniot jump relations result, as it should.

5

In this hydrodynamic description the flame propagation is affected by the local mixture properties (through the Markstein length) and by the flow conditions (through stretching), while the flow field is modified by gas expansion. In an experimental setting, changes in the Markstein length are accommodated by varying the fuel type and/or mixture composition (through the effective Lewis number and heat release parameter), or by varying the system pressure (through the flame thickness l_f).

The hydrodynamic model which, fully accounts for thermal expansion, allows for folded flames, and contains the full contribution of flame stretch including curvature and hydrodynamic strain, differs from the so-called "G-equation" approach, where one or more of these effects are typically missing [47–51]. Although the G-equation used for tracking the flame is similar to (11), studies using this approach have often resorted to a prescribed velocity field not affected by combustion, described the flame by a single-valued function that does not allow for folding and detachment, or assumed that the flame propagates either at a constant speed or with dependence on flame front curvature only. Exceptions are the general formulation given by Kerstein et al. [52], and the studies of Peters [53] and Pitsch and Duchamp De Lageneste [54], Pitsch [55] carried out within RANS and LES context, i.e., averaging or filtering the G-equation with closure assumptions for the correlation terms or for the sub-grid variance of G-function. In these formulations, however, the scalar-strain covariance accounting for the variations between fluctuations in the G-term and hydrodynamic straining, was shown to be most effective at scales on the order of the Markstein length $\mathscr{L}$, and was therefore neglected. Studies using the G-equation have predominantly excluded the effect of hydrodynamic strain which, as discussed below, has a greater effect on the turbulent flame speed than curvature.

2.2. Numerical methodology

The numerical implementation of the hydrodynamic model is carried out using a hybrid NS/front-tracking scheme, with a pre-generated homogeneous, isotropic, turbulent flow swept at the inflow with velocity v_{in}, as described in [46]. The NS equations (13a)-(13b), are integrated in a two-dimensional domain of transverse dimension L, with periodic boundary conditions imposed in the spanwise direction. The equations are integrated in their dimensionless form with length, speed and time scaled by L, S_L and L/S_L, respectively, and ρ, μ scaled by their unburned values. The solver used is a modification of the parallel low Mach number variable-density solver devel-

oped at Lawrence Berkeley National Laboratory [56] that properly accommodates for the source term in the mass conservation equation. The flame surface is tracked via the level-set equation (11), with the inflow velocity v_{in} adjusted via a closed loop control system to keep the mean flame position at a fixed location and retain the turbulence intensity at a specified value in the vicinity of the flame. A novel aspect in this work is the implementation of an improved front tracking technique that can numerically parametrize both, multivalued and disjointed interfaces, which allows extending the calculations to higher values of turbulence intensities. The new algorithm, inspired from the method proposed in [57], is described in the Appendix. The vertical dimension is appropriately selected to accommodate the flame fluctuations at high turbulence intensities. The numerical thickness h is taken as three-to-four cell size, in order to retain the piecewise behavior of the density function (12). The investigated resolutions were 128 to as low as 64 points per unit length; the lower resolutions were typically used for expediency, noting that at the highest resolution the variation in the value of turbulent flame speed was less than 4%. The accuracy of the numerical scheme has been established both in laminar and turbulent settings by reproducing with sufficient numerical precision the bifurcation characteristics of premixed flames, known analytically from closed-form dispersion relations, and the exact pole solutions of the weakly non-linear Michelson-Sivashinsky equation [58–60].

The turbulent flow introduced at the inflow, see Fig. 1, is obtained by evolving through the incompressible NS equations with density ρ_u an initial realization based on an energy spectrum function, in a box with periodic boundary conditions imposed on all boundaries, as discussed in [46]. The vertical dimension of the domain was 64 times the transverse dimension, in order to allow for sufficient statistical significance. The generated turbulent flow is characterized by an intensity v_c', defined as the root-mean-square of the velocity fluctuations, and an integral length scale ℓ identified as a mean representation of two-point velocity correlation. The intensity v_c' represents the turnover velocity of the energy-carrying eddies of size ℓ. More relevant to turbulent flames is the Gibson scale $\ell_G \sim \ell \, (v_c'/S_L)^{-3}$, which corresponds to a turnover velocity on the order of the laminar flame speed [43]. We assume that only eddies of size larger than ℓ_G are able to wrinkle and fold the flame surface, while eddies of much smaller size, all the way to the Kolmogorov scales, are not energetic enough to interact with the flame and have a negligible effect on its propagation. The flame thick-
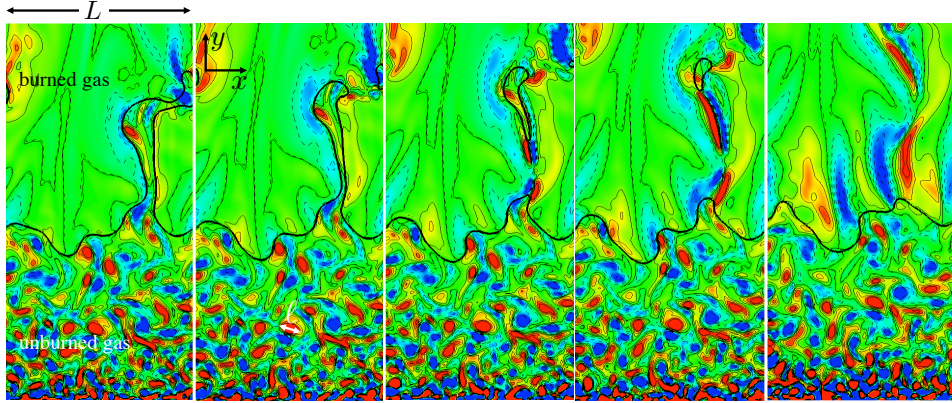
Figure 1: Representative solution of a statistically stationary turbulent flame (solid dark curve) held at mid-height location, at consecutive times; calculated for $\sigma = 5$, $\mathcal{M} = 0.018$, $v'_c = 1.4$, $\ell = 0.1$. The turbulent flow is illustrated by vorticity contours with (red/blue) solid/dashed curves corresponding to positive/negative vorticity values.

ness l_f in the hydrodynamic model is the smallest length scale in the system and the inner flame structure remains locally as that of a laminar flame experiencing a stretch rate determined by the local flow conditions. The flame-turbulence interactions are therefore advective/kinematic in nature, and one needs only resolve the Gibson scales, while the smaller scales can go safely unresolved. The calculations presented below correspond to $\ell/L = 0.1$, and for $0 < v'_c/S_L \leq 2$ the Gibson scale $\ell_G/L \gtrapprox 0.0125$ is within the range of scales resolved by the high resolution calculations (where the smallest resolved scale is 0.015625), and is in most cases within the range of scales resolved with the coarser resolution.

Similar to all other diffusion processes, the viscous term in (13b) is $O(\delta)$, implying that the Reynolds number $Re = \rho_u L S_L/\mu_u = (\delta Pr)^{-1}$, where Pr is the Prandtl number, is large. In the calculations reported below we have taken $Re = 2 \cdot 10^3$ and kept μ constant (independent of temperature). Increasing the Reynolds number to $Re = 10^5$ had a minor effect on the results, typically less

$\mathcal{M}$	v'_c/S_L	S_T/S_L $Re = 2 \cdot 10^3$	S_T/S_L $Re = 10^5$	% diff
0.0333	0.2	1.1609	1.1526	0.71%
	0.8	1.3386	1.3409	0.17%
	1.2	1.4584	1.4528	0.38%
0.0267	0.1	1.2016	1.1952	0.54%
	0.8	1.4096	1.4079	0.12%
	1.2	1.5733	1.5614	0.76%

Table 1: Effect of varying the Reynolds number on the turbulent flame speed, for two representative Markstein numbers $\mathcal{M}$ and several values of the turbulent intensity v'_c.

than 1% difference, as illustrated in Table 1. The main role of the viscous term in our model is infusing a small degree of dissipation in the system for the numerical computations, and the results presented in Table 1 simply imply that the flame behavior is not sensitive to the degree of dissipation introduced. Variations in Reynolds number do not noticeably affect the dissipative process occurring from the inflow to the flame zone nor do they ultimately affect the turbulent propagation speed which remains uniquely dependent upon the parameters characterizing the inflow turbulence, namely intensity and integral scale.

The simulations presented below cover the range of turbulent intensities $0 < v'_c/S_L \leq 2$, with the integral length scale set to $\ell/L = 0.1$ and the thermal expansion parameter $\sigma = 5$. The dependence of flame characteristics on the integral scale ℓ and thermal expansion parameter σ and ℓ have been partially reported in [46, 61] and will be further discussed in a sequel. We have also limited the discussion to mixtures with positive values of Markstein length, where the flame is not contaminated by thermo-diffusive instabilities. Since the flame thickness l_f is only introduced implicitly through the Markstein length, the Markstein number has been defined relative to the domain of integration L, namely $\mathcal{M} = \mathcal{L}/L$. It differs from the conventional definition of Markstein number based on the flame thickness by a factor $\delta = l_f/L$. In Table 2 we provide values of the conventional Markstein number $\mathcal{L}/l_f$ for H_2-air and C_3H_8-air mixtures over a range of equivalence ratios, calculated using the expression provided in [40] for constant transport properties. Also provided in the table are values of the corresponding Markstein number $\mathcal{M}$ based on the current-definition, for two rep-

<center>H₂-air mixtures</center>

ϕ	σ	Le_{eff}	l_f(mm)	$\mathscr{L}/l_f$	$\mathscr{L}$(mm)	$\mathscr{L}^{\text{b}}$(mm)	$\mathcal{M}$ $\delta=0.01$	$\mathcal{M}$ $\delta=0.02$
0.50	5.0	0.53	0.0652	0.9030	0.0589	-0.0461	0.0090	0.0181
0.75	6.2	0.82	0.0253	1.8820	0.0475	0.0016	0.0188	0.0376
1.00	6.9	1.33	0.0187	2.6640	0.0497	0.0138	0.0266	0.0533
1.25	6.8	1.67	0.0170	2.9820	0.0508	0.0182	0.0298	0.0596
1.50	6.5	1.81	0.0171	3.0340	0.0519	0.0198	0.0303	0.0607
1.75	6.3	1.90	0.0182	3.0650	0.0558	0.0223	0.0307	0.0613
2.00	6.1	1.96	0.0199	3.1000	0.0616	0.0258	0.0310	0.0620

<center>C₃H₈-air mixtures</center>

ϕ	σ	Le_{eff}	l_f(mm)	$\mathscr{L}/l_f$	$\mathscr{L}$(mm)	$\mathscr{L}^{\text{b}}$(mm)	$\mathcal{M}$ $\delta=0.01$	$\mathcal{M}$ $\delta=0.02$
0.8	7.2	1.59	0.0721	3.5548	0.2563	0.1144	0.0356	0.0711
1.0	8.3	1.36	0.0507	3.0477	0.1545	0.0470	0.0305	0.0610
1.2	8.1	1.16	0.0493	2.6798	0.1321	0.0290	0.0268	0.0536
1.4	7.9	1.08	0.0717	2.5162	0.1804	0.0324	0.0252	0.0503
2.0	7.3	0.99	0.4899	2.2825	1.1180	0.144	0.0228	0.0460

Table 2: Values of the conventional Markstein number $\mathscr{L}/l_f$ for H₂-air and C₃H₈-air mixtures over a range of equivalence ratios, and the corresponding Markstein number $\mathcal{M}$ based on the current-definition, for two representative values of δ.

resentative values of δ. The values of density ratio, flame thickness and Markstein length (based on the corresponding effective Lewis Le_{eff}), were taken from [62] for the H₂-air mixtures and from [41] for the C₃H₈-air mixtures. We have also included in the table the burned Markstein length $\mathscr{L}^{\text{b}}$ which, as discussed in [41], is the appropriate value that must be used for comparison with experiments and simulations[1]. We observe that the range of Markstein number considered in this work, $\mathcal{M} \sim 0.05 - 0.018$, could be associated with H₂-air or C₃H₈-air mixtures. The data also provides the estimate $\ell/l_f \sim 10 - 20$ which allows locating our results in the classical turbulent combustion regime diagram. For the range of turbulence intensities we have considered ($v'_c/S_L \sim 0 - 2$) our results fall in the wrinkled-to-corrugated flamelets regimes of the classical turbulent regime diagram.

3. Flame topology

The representative calculations shown in Fig. 1 correspond to turbulent flame at five consecutive times, prop-

agating (downwards) against a turbulent flow of intensity $v'_c/S_L = 1.4$ supplied at a rate v_{in} at the bottom of the domain. The combustible mixture is characterized by $\sigma = 5$ and $\mathcal{M} = 0.05$. The flame surface represented by a solid black curve is held stationary (on the average) at mid-height location by controlling v_{in}, which is therefore equal to the mean propagation velocity of the turbulent flame, or S_T. The turbulent flow is represented by vorticity contours, with (red/blue) solid/dashed curves corresponding to clockwise/counterclockwise rotation. The sequence clearly illustrates the deformation of the flame by the turbulence, flame folding and pinching, detachment of a pocket of unburned gas and its rapid consumption. The reduction of the turbulence level in the hot burned gas that results from gas expansion is also evident. Further details and quantification of these observations will be given below.

3.1. Regimes of turbulent flame propagation

For low values of the turbulence intensity Creta and Matalon [46] have identified two distinct regimes of flame propagation: a *sub-critical regime* where, on the average, the flame brush remains planar (i.e., has zero mean curvature) and the fluctuating flames are unaffected by the DL instability, and a *super-critical regime* where the flames frequently attain a distinct cusp-like conformation, reminiscent of hydrodynamically unstable flames under

---

[1]The Markstein length $\mathscr{L}$ is a representative value that mimics the reaction and diffusion processes inside the flame zone, and must be only used in the asymptotic context when the flame shrinks to a surface. Expressions for the Markstein length at different reference locations inside the flame zone can be found in [41]; in particular, $\mathscr{L}^{\text{b}}$ corresponds to the value on the burned side of the flame.

<center>8</center>

(a) $\mathcal{M} = 0.05$ (sub-critical conditions)

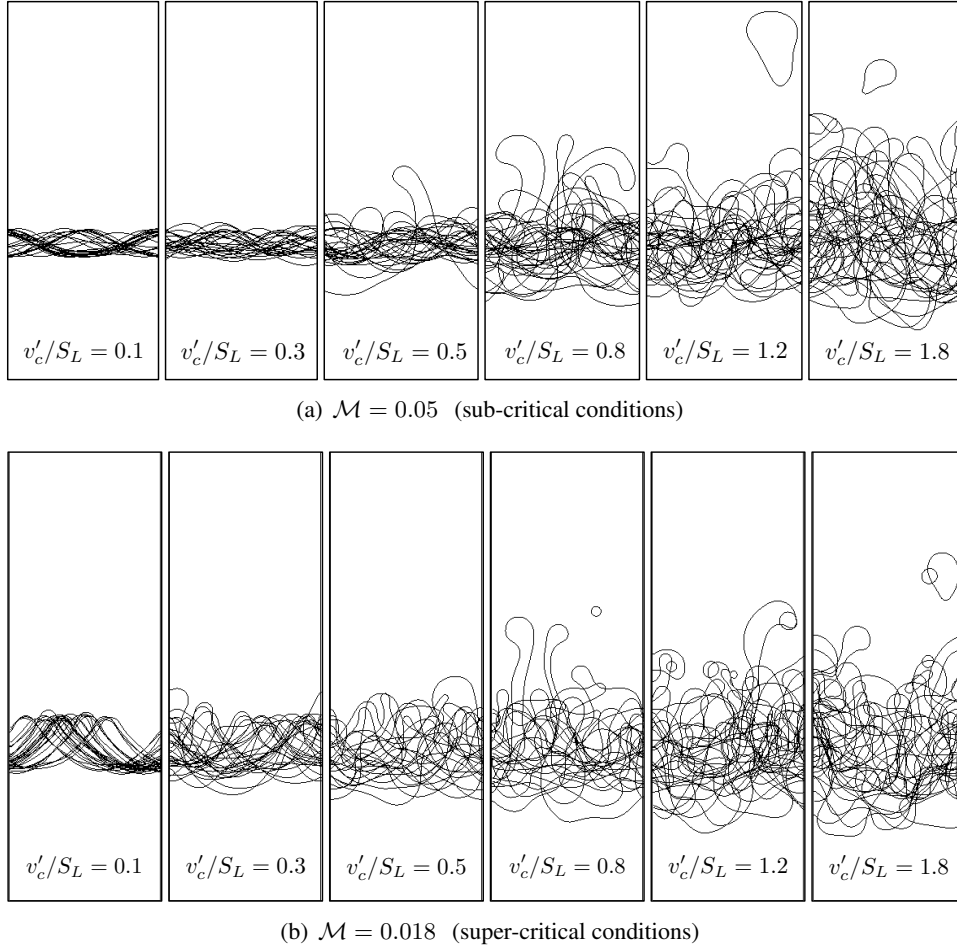(b) $\mathcal{M} = 0.018$ (super-critical conditions)

Figure 2: Flame brush at increasing values of turbulence intensity for sub- and super-critical conditions.

laminar conditions, giving the flame brush a robust appearance that seems hardly affected by the turbulence. This classification, in analogy to the characterization of stable/unstable regimes of laminar flames, is based on whether the Markstein number $\mathcal{M}$ is above/below the critical value

$$\mathcal{M}_c = \frac{(\sigma - 1)}{2\pi(3\sigma - 1)} \qquad (14)$$

determined from linear stability theory [59]. For $\sigma = 5$ considered here, the critical Markstein number $\mathcal{M}_c = 0.0454$. These two regimes are clearly seen in Fig. 2, as described below.

Plotted in Fig. 2 are sets of instantaneous snapshots of the fluctuating flames superimposed on each other at a mean location, for two values of $\mathcal{M}$ and increasing values of the turbulence intensity v'_c. The vertical extent of the flame profiles represents the turbulent flame brush. For $\mathcal{M} = 0.057 > \mathcal{M}_c$, classified as sub-critical, the turbulent flame at low turbulence intensities is unaffected by the DL instability and the flame brush remains nearly planar. As v'_c increases, the flame brush thickens with flames expe-

riencing larger and larger fluctuations and developing frequent folds. At values of $v'_c/S_L > 1$ the flames are highly convoluted and bear no resemblance to the nearly planar conformations observed at low turbulence intensity. For $\mathcal{M} = 0.018 < \mathcal{M}_c$, classified as super-critical, the turbulent flame at low turbulence intensities is highly corrugated with pointed crests intruding into the burned gas and wide rounded troughs towards the unburned gas. This robust appearance, reminiscent of the cusp-like structures that develop as a result of the DL instability, is hardly affected by the turbulence. As v'_c increases the flame surface develops folds that pinch-up, forming pockets of unburned gases that detach from the main flame surface and are rapidly consumed. At sufficiently large values of v'_c the cusp-like structures are no longer visible and the overall flame brush loses the distinguished appearance that characterized the low-intensity flames. At sufficiently high turbulence levels, $v'_c/S_L \gtrsim 2$ say, the flame brush for the two Markstein numbers seem indistinguishable from each other. In this *highly-turbulent regime* the influences of the DL instability have apparently decreased to such an
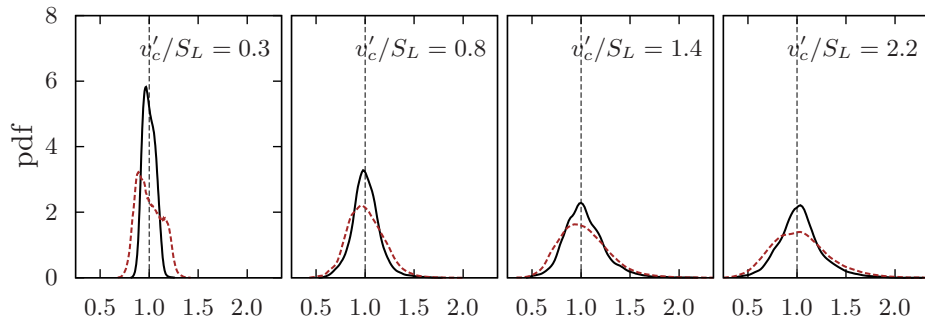
(a) Probability density function of flame position
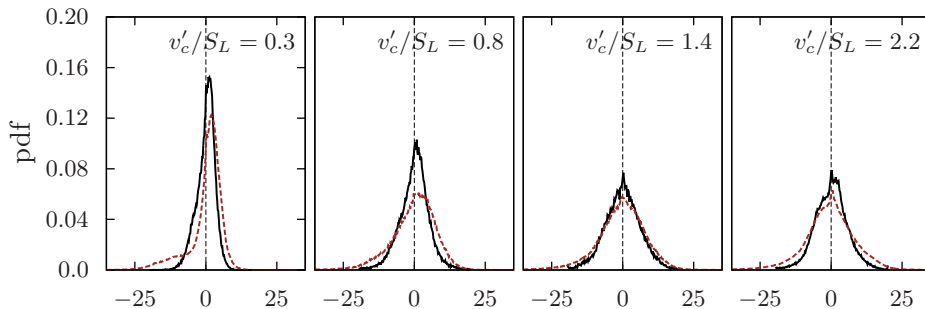
(b) Probability density function of flame curvature

Figure 3: Probability density functions of flame position and curvature parametrized with v'_c/S_L for two values of Markstein number, $\mathcal{M} = 0.05$ (black/solid), 0.018 (brown/dashed) corresponding to sub- and super-critical conditions, respectively.

extent that it has no longer a visible effect on the turbulent flames. These observations will be further examined below based on the statistical flame characteristics.

3.2. Characterization of flame brush topology

To characterize flame brush topologies we examine in Fig. 3 the probability density functions (p.d.f.'s) of flame position and curvature for the two values of Markstein numbers used in the illustrations of Fig. 2. Focusing first on sub-critical conditions, $\mathcal{M} = 0.05$, we observe that for low values of the turbulence intensiy the p.d.f. of the flame position is narrow and symmetric about the mean (here $y = 1$). The flame curvature p.d.f. exhibits similar characteristics; it is also symmetric with zero mean, confirming that the flame brush is indeed planar on the average. These results are consistent with our previous communication [46]; the slight asymmetry of the mean curvature towards positive values seen in the figure for $\mathcal{M} = 0.05$, which for the value $\sigma = 5$ considered here is close to $\mathcal{M}_c = 0.0454$, is due to the DL instability shown to have already some influence on the flame at near criticality [61]. As the turbulence intensity increases, the p.d.f. of the flame position remains symmetric but widens indicating a thicker flame brush. The curvature p.d.f. also widens encompassing

a larger range of positive and negative curvatures, while staying symmetric with zero mean.

In contrast, both p.d.f.'s for super-critical conditions ($\mathcal{M} = 0.018$) have, at low turbulence intensity, a clear asymmetric shape as illustrated in the figure for $v'_c/S_L = 0.3$. The bimodal shape of the p.d.f.'s is a direct consequence of the distinct flame conformation that emerges as a result of the DL instability, with highly-peaked crests (intruding into the burned gas) and much wider and rounded troughs. The peak of the curvature p.d.f., corresponding to small positive curvatures, arises from the rounded troughs of the flame surface, and the large negative curvatures correspond to the highly pointed crests. As the turbulence intensity is increased, the flame position and curvature p.d.f.'s for $\mathcal{M} = 0.05$ spread out and the one for $\mathcal{M} = 0.018$ lose their bimodal character, regaining symmetrical but much wider shapes. The widening of the p.d.f.'s indicates the formation of a thicker flame brush and a wider range of curvatures acquired by the flame. The gradual loss of their distinct asymmetric shapes as v'_c is increased is an indication of a diminishing influence of the DL instability. For sufficiently high values of v'_c, we have seen (Fig. 2) that the flame brush for the

two Markstein numbers become indistinguishable; hence, their p.d.f.'s tend towards nearly identical shapes. The flame position p.d.f. is again symmetric but its shape is much wider with a long tail extending towards the burned side of the flame. The curvature p.d.f. is also symmetric about the mean, which is slightly negative, and a long tail with respect to negative curvatures. These tails are indicative of intermittent formation of long intrusions into the burned gas and detachment of flame pockets from the flame surface, as readily deduced from the following post-analysis of snapshots of the flame surface. Shown in Fig. 4 is the instantaneous flame profile right after a pocket of unburned gas has pinched up from the main flame surface, along with the local flame curvature κ for each segment, plotted as a function of the flame coordinate s (measured along the arc length). Examining the values of κ for each flame segment shows that the high negative local curvatures of the pocket and the intrusion correlate well with the values observed at the tail of the curvature p.d.f.s.

The wide symmetrical p.d.f.'s of flame position with long tails extending towards the burned gas region along with the wide symmetrical curvature p.d.f.'s with negative mean curvature and long negative tails, are quite distinct from the p.d.f.'s observed in the sub- and super-critical regimes; they clearly characterize the new highly-turbulent regime identified earlier. Similar p.d.f.'s were
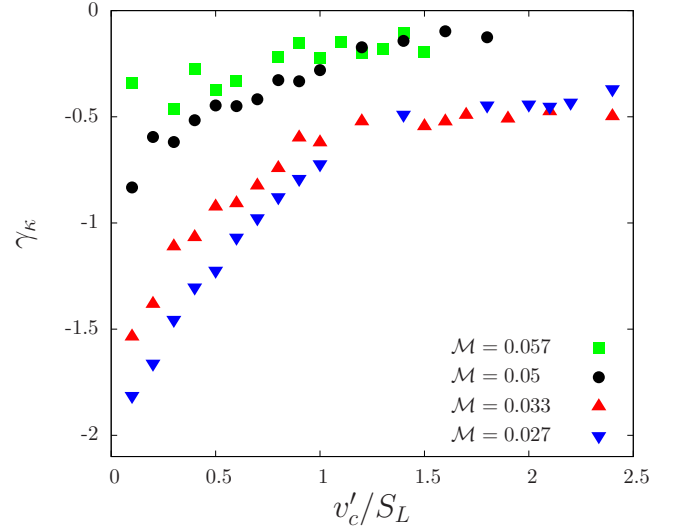
Figure 5: Variation of skewness of the curvature p.d.f.s γ_κ with turbulence intensity for values of Markstein number above/below the critical value $\mathcal{M}_c = 0.0454$.

reported in experimental and simulation studies. Symmetric p.d.f.'s of flame curvature were reported in [63] and [64] based on experiments of turbulent propane/air flames subjected to intensities v'_c/S_L ranging from 1.42 to 5.7, that could be considered in the highly-turbulent regime. Three mixtures with Lewis numbers $Le = 1.86, 1.40, 0.98$ were examined, which can be correlated to distinct values of $\mathcal{M}$ (in decreasing order). Variation in Le were found to have no effect on the curvature p.d.f.'s in accord with our predictions. Long tailed p.d.f.'s of flame position extending towards the burned gas were reported in [65] from simulations based on a G-equation approach with a constant flame speed (for $\sigma = 5$ and $v'/S_L = 2.35$), and long negative-tailed curvature p.d.f. were reported in [66] from two-dimensional simulations of a methane-air flame based on a reduced chemical mechanism and a simplified transport model (for $v'_c/S_L = 4.2$).

The distinction between the different regimes identified earlier can be ascertained by examining the skewness of curvature γ_κ, which measures the asymmetry of the corresponding p.d.f. about its mean. Plotted in Fig. 5 is the variation of γ_κ with increasing values of turbulence intensity, for four different values of Markstein numbers. The contrast between the skewness of flames with $\mathcal{M} < \mathcal{M}_c$ from those with $\mathcal{M} > \mathcal{M}_c$ at low values of turbulence intensity, is quite evident; the super-critical regime have larger negative skewness as compared to the small values in the sub-critical regime. For larger values of turbulence intensity however, $\gamma_\kappa \to 0$ for all values of $\mathcal{M}$, indicating symmetric distribution of curvatures and the emer-
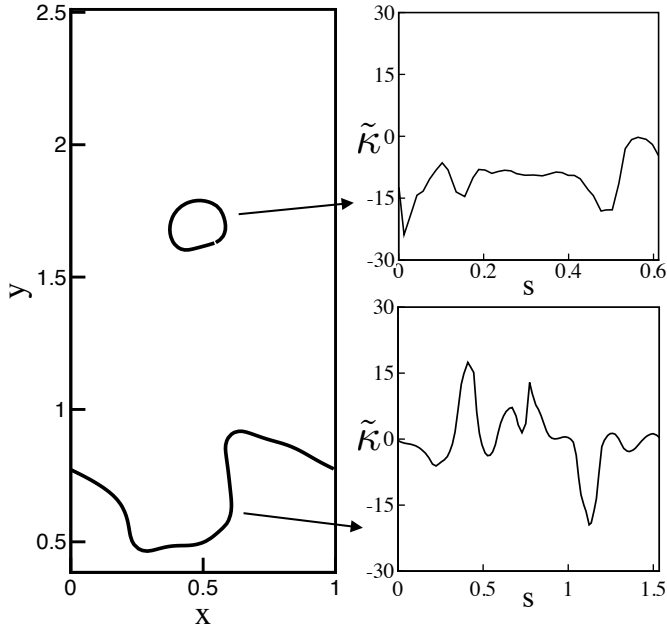

Figure 4: Plotted on the left is a snapshot of an instantaneous flame profile, containing an intrusion and a pocket of unburned gases; taken from the simulations with $\mathcal{M} = 0.033$ and $v'_c/S_L = 1.4$. Plotted on the right is the dimensionless curvature $\tilde{\kappa} = L\kappa$ along the flame coordinate s for each of the two flame segments.
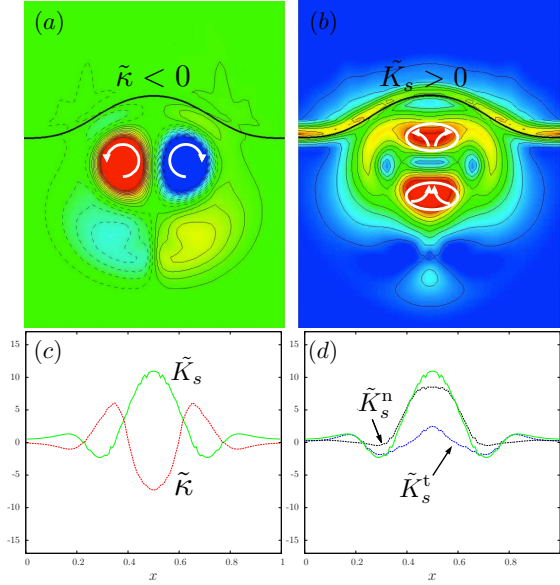
Figure 6: The distortion of a planar flame by a vortex pair simulated for $\sigma = 5$ and $\mathcal{M} = 0.057$; the flame surface is represented by the solid black curve. (a) Contours of constant vorticity, with red/blue for positive/negative vorticity, illustrating the vortex pair, (b) Contours of constant strain rate magnitude E showing the straining nature experienced by the flame, (c) Variations of the dimensionless curvature $\tilde{\kappa} = L\kappa$ and strain rate $\tilde{K}_s = LK_s/S_L$ along the flame, (d) Variations of the normal and tangential components of strain rate, $\tilde{K}_s^{\mathrm{n}}$ and $\tilde{K}_s^{\mathrm{t}}$ respectively, along the flame.
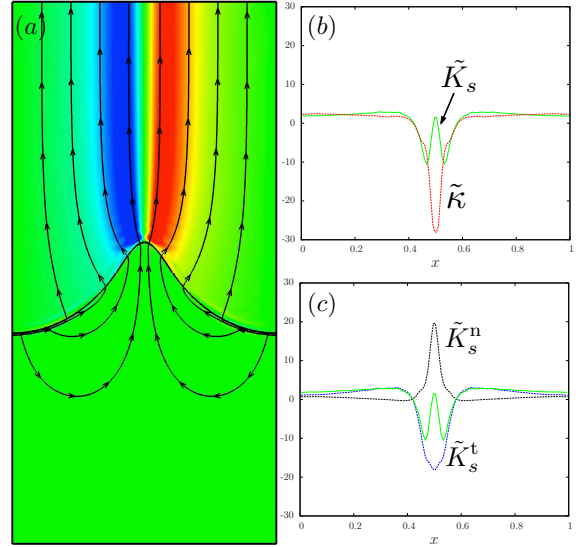

Figure 7: The distortion of a planar flame as a result of the DL instability, calculated for $\sigma = 5$, $\mathcal{M} = 0.027$; the flame surface is represented by the solid black curve. (a) Nature of the flow field across a steadily propagating cusped-like flame (propagating downwards at a speed U_L); illustrated by selective streamlines. Also shown is the magnitude of vorticity (in different grey shades or red/blue for positive/negative values) produced at the flame and convected downstream. (b) Variations of the (dimensionless) curvature and strain rate along the flame (c) Variations of the (dimensionless) normal and tangential components of the strain rate K_s along the flame.

gence of the highly-turbulent regime. A similar trend was also reported in [64] in their experimental results examining the wrinkling of spherically expanding iso-octane and methane flames at turbulence intensities $v_c'/S_L \approx 1 - 11$.

Since the main distinction between the sub- and super-critical regimes is whether the DL instability affects the turbulent propagation, the skewness also serves as a measure of the DL influence, as proposed by Troiani et al. [28] who observed in their experiments with Bunsen propane/air flames a similar increase in γ_κ (from negative values towards zero) with diminishing DL influences. A decrease in γ_κ with increasing Lewis numbers for mixtures with $Le > 1$, equivalent to an increase in $\mathcal{M}$, at an intensity of $v_c'/S_L \approx 1$ was reported in a DNS study of premixed turbulent flames [67] assuming a constant density flow but non-unity Lewis numbers.

3.3. Curvature – Strain correlation

Another quantity used to characterize flame – turbulence interaction is the correlation between the curvature of the flame surface κ and the strain rate experienced by the flame K_s. A turbulent flame is typically strained by velocity gradients caused either due to turbulence or due to the flow induced in the unburned gas as a result of the DL instability. These two distinct mechanisms can be illustrated by considering the following two models: (i) the interaction of a laminar flame with a vortex pair, and (ii) the nonlinear development of a hydrodynamically unstable laminar flame, as suggested by Steinberg et al. [68]. The first has been utilized in numerous studies, both experimental [69, 70] and computational [71–73], to characterize flame – turbulence interaction; the second is a direct examination of the nonlinear consequence of the DL instability [59, 74]. These two configurations, which were simulated numerically by considering the distortion of a planar laminar flame subjected to a pair of counter-rotating vortices or to the DL instability, are discussed next.

Figure 6 shows the interaction of a nominally planar flame with a pair of counter rotating vortices leading to a distorted flame surface of predominantly negative curvature (except near the two sides of the domain). Contours of constant vorticity and overall strain rate are shown in Fig. 6(a) and Fig. 6(b), respectively. The magnitude of the overall strain rate is determined from $E = (e_{ij}e_{ji})^{1/2}$, where e_{ij} are the elements of the strain rate tensor $\mathbf{E}$, with the summation convention adopted. Marked on the graph of Fig. 6(b) are the flow patterns responsible for exten-

12

(a) $\mathcal{M} = 0.057$ (sub-critical conditions)   (b) $\mathcal{M} = 0.033$ (super-critical coditions)
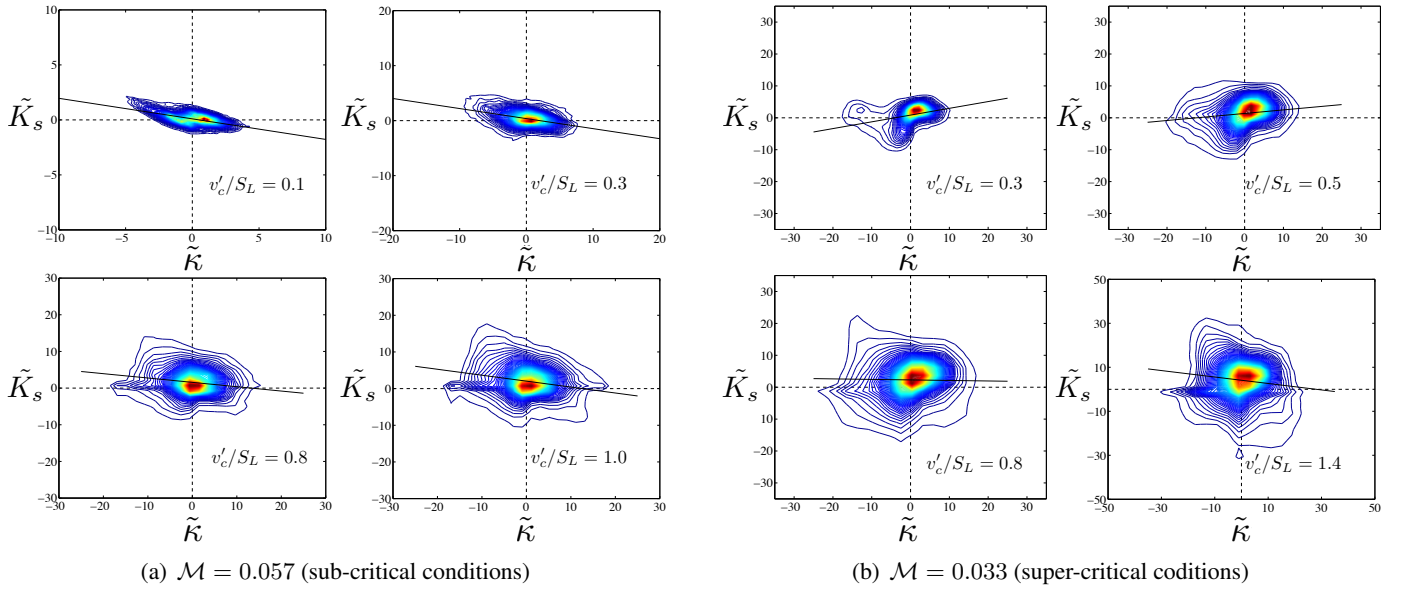
Figure 8: Joint p.d.f. of flame curvature and strain rate for increasing values of turbulence intensity and two distinct values of Markstein number.

sive and compressive straining of the flame surface, where it becomes evident that the negatively curved flame segment is positively stretched; see also [75]. The computed profiles of the strain rate K_s and flame curvature κ along the flame surface are shown in Fig. 6(c). Also shown in Fig. 6(d) are the normal $K_s^n = -v_n\kappa$ and tangential $K_s^t = \nabla_\tau \cdot \mathbf{v}_\tau$ components of the strain rate experienced by the flame. Along the negatively curved segments of the flame, both components of K_s contribute towards extensive (positive) straining; they contribute towards compressive (negative) straining at the positively curved regions [59]. Hence, as the flame interacts with a vortex pair, or equivalently due to turbulence, negatively curved segments experience extensive (positive) straining while positively curved flame segments experience compressive (negative) straining.

Figure 7 shows the steadily propagating structure that develops when a planar laminar flame becomes hydrodynamically unstable. Flame straining in this scenario occurs as a result of the flow induced in the unburned gas by gas expansion. The flow field is illustrated in Fig. 7(a) with selected streamlines and contours of vorticity, which is produced at the flame and convected downstream. The computed profiles of the strain rate K_s and flame curvature κ along the flame surface are shown in Fig. 7(b). At the negatively curved crest the normal and tangential components of the strain rate K_s have opposite effects [59], as illustrated in Fig. 7(b), resulting in an overall net compressive effect ($K_s < 0$), except in a narrow region near the highly-curved tip of the flame where K_s reverts back

to very small positive values. At the positively curved troughs, the strain components act synergistically, leading to a net extensive effect ($K_s > 0$). Hence, as a result of the DL instability, negatively curved segments experience compressive (negative) straining while positively curved flame segments experience extensive (positive) straining.

To examine the extent of the aforementioned two mechanisms in straining a turbulent flame, we have plotted in Fig. 8 the joint p.d.f. of flame curvature and strain rate at increasing values of turbulence intensity, for two distinct values of Markstein number; $\mathcal{M} = 0.057$ and $\mathcal{M} = 0.033$ corresponding to sub- and super-critical conditions, respectively. Fig. 8(a) corresponds to sub-critical conditions where the DL mechanism is absent and the primary mechanism of flame straining is via turbulence. Indeed, for all values of v_c', negatively curved segments are subjected to positive (extensive) straining and vice versa, consistent with the results of the idealized model of a planar flame interacting with a pair of counter-rotating vortices. A linear fit of the form $K_s = a + b\,\kappa$ to the curvature-strain data results in a negative slope ($b < 0$) for all turbulence intensities, as shown in the figure. The 2D simulations of Haworth and Poinsot [76] for three values of Lewis number, $Le = 0.8, 1.0, 1.2$, with turbulence intensity $v_c'/S_L \approx 5$, and the 3D simulations of Chakraborty and Cant [77] for $Le = 1.0$ with $v_c'/S_L = 7.2$ yielded similar negative correlations between flame curvature and strain rate. A similar behavior was noted in the experiments of Renou et al. [78] with stoichiometric CH_4-air, and lean H_2-air expanding flames at turbulence intensities, $v_c'/S_L = 0.46$
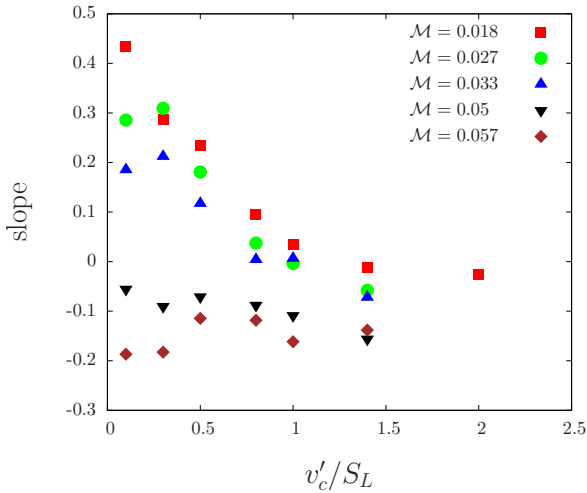
13

Figure 9: Variation of the slope of the linear fit to curvature-strain joint p.d.f. data with increasing turbulence intensity for different Markstein numbers.

(a)

(b)

Figure 10: Schematic of (a) a statistically stationary turbulent premixed flame, and (b) a multi-valued segment of the flame surface.

and $v_c'/S_L = 0.95$ respectively.

Figure 8(b) corresponds to super-critical conditions where the DL instability plays a significant role, at least at low values of v_c'. Indeed, for $v_c'/S_L \sim 0.3$, the joint p.d.f. shows that negative curvatures are associated with compressive (negative) straining and vice versa, consistent with the corrugated flame structure that results from the DL instability. The high negative values of curvature ($\kappa \sim -15$) associated with very small strain rate values, are a consequence of the negatively curved crests that arise frequently on the flame surface as a result of the instability, as already seen in Fig. 2. In fact, at these crests, a local anticorrelation between curvature and strain may tend to emerge, where local values of strain may revert to being positive as observed on Fig. 7 (b) and (c). The linear fit $K_s = a + b\,\kappa$ drawn for the curvature-strain data at low turbulence intensities, results here in a positive value of the slope b. As turbulence intensity increases, $v_c'/S_L = 0.5, 0.8$ say, the slope b starts to decrease and tend towards zero, indicative of the fading influence of DL instability. At $v_c'/S_L = 1.4$, the slope b has a negative value, suggesting that the DL straining mechanism has completely been overshadowed by turbulence.

The variation in slope b with turbulence intensity is shown in Fig. 9 for several values of the Markstein number. For $\mathcal{M} = 0.057, 0.05$, both in the sub-critical regime, the slope $b < 0$ for all values of turbulence intensity, indicating that the primary mechanism for flame straining is the interaction with turbulence. For $\mathcal{M} = 0.033, 0.027, 0.018$, all in the super-critical regime, the slope $b > 0$ for low turbulence intensities; it tends towards zero as v_c' increases reverting eventually to a nega-
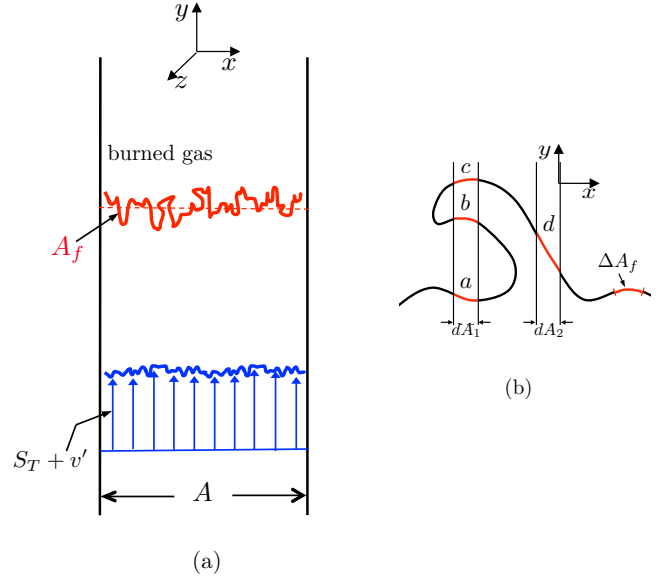
tive value. The primary mechanism for flame straining at low turbulence intensities is therefore the DL mechanism, but its influence fades away as v_c' increases with the flame becoming controlled by the turbulence at sufficiently high turbulence levels. This behavior further supports the existence of a highly-turbulent regime in which DL effects have minimal influence on turbulent flame propagation. Therefore, similar to the skewness of curvature p.d.f., the slope of the linear fit $K_s = a + b\kappa$ to the curvature-strain joint p.d.f. data can also be used as a measure of the influence of DL instability. It must be noted however, that the linear fit and its slope are merely used as markers for the presence of DL effects. In general, the relation between curvature and strain is non-linear as evident from Fig. 8.

4. Turbulent flame speed

The turbulent flame speed S_T may be defined as the mean propagation speed of a premixed flame into a (statistically homogeneous) turbulent gas mixture of zero mean velocity and uniform mean properties, in analogy to the laminar flame speed defined as the propagation speed of a premixed flame into a quiescent uniform mixture. The direction of propagation, defined as the direction perpendicular to the mean flame location, is assumed along the y-axis. In a coordinate system moving with the mean flame position, the flame remains statistically stationary and the mean incident flow velocity through a cross section of area A is equal to S_T, as shown schematically in Fig. 10(a).

Following Damköhler [4] an expression for the turbu-

14

lent flame speed can be obtained from an overall mass conservation statement. The mean (in time and cross sectional area) mass flow rate towards the flame is given by

$$\overline{m} = \rho_u S_T A$$

If all the reactants introduced at the inlet pass through the wrinkled flame, $\overline{m}$ can be also calculated from the total mass flowing through the area elements ΔA_f comprising the flame surface. Assuming each element of the flame surface propagates at a speed S_f,

$$\overline{m} = \lim_{\Delta t \to \infty} \frac{1}{\Delta t} \int_{t}^{t+\Delta t} \lim_{A \to \infty} \left\{ \frac{1}{A} \iint (\rho_u S_f \Delta A_f) \, dA \right\} dt$$

resulting in an expression for the turbulent flame speed as $S_T = \overline{S_f(A_f/A)}$, where the "overline" denotes the average in time and cross sectional area, i.e, for a quantity φ defined on the flame surface

$$\overline{\varphi} = \lim_{\Delta t \to \infty} \frac{1}{\Delta t} \int_{t}^{t+\Delta t} \lim_{A \to \infty} \left\{ \frac{1}{A} \iint \varphi \, dA \right\} dt \, . \quad (15)$$

It should be noted that when integrating over a particular element of cross sectional area dA where the flame surface is multiply folded, all contributions of φ within dA need to be included; see also [52]. Hence, φ in (15) must be interpreted as the sum of this quantity over all flame area elements within the differential cross sectional area dA, as illustrated in Fig. 10(b). For the element dA_1, the integrand would include $(\varphi_a + \varphi_b + \varphi_c)dA_1$ whereas for the element dA_2 it would simply be $\varphi_d dA_2$.

At any point of the flame surface, the ratio of the area element of the flame surface to the projected area element along the direction of propagation can be expressed in terms of the function $\psi(\mathbf{x}, t)$, such that

$$\frac{\Delta A_f}{\Delta A} = \frac{|\nabla \psi|}{|\mathbf{j} \cdot \nabla \psi|}$$

where $\mathbf{j}$ is a unit vector in the y-direction, with the understanding that the gradient is evaluated at $\psi = 0$; see Williams [79, page 430]). The turbulent flame speed is then given by

$$S_T = \overline{\frac{S_f A_f}{A}} = \overline{S_f \frac{|\nabla \psi|}{|\mathbf{j} \cdot \nabla \psi|}} \, . \quad (16)$$

This expression shows that the increase in speed of the turbulent flame includes contributions other than the in-
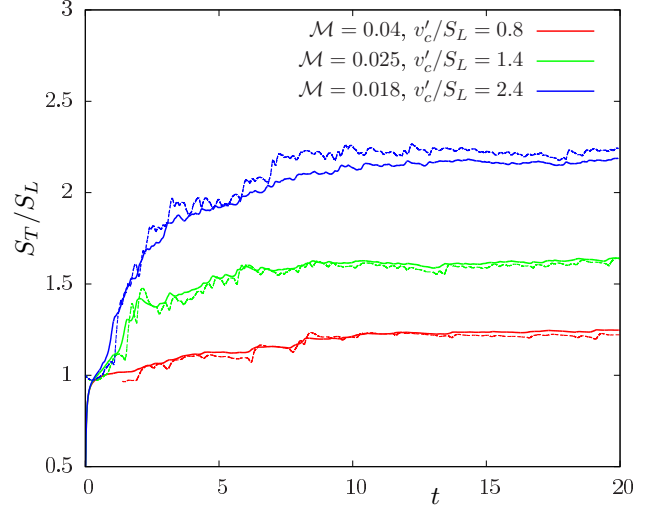

Figure 11: Comparison of the turbulent flame speed evaluated based on Eq. (16) - solid lines - or as the mean inflow velocity - dashed lines, for selected values of the parameters. The graph shows the transient solution obtained via the control system until the flame reaches a statistically stationary state.

crease in surface area envisaged by Damköhler who, by assuming that all elements of the wrinkled flame propagate at a constant speed equal to S_L, obtained the relation $S_T/S_L = \overline{A_f}/A$.

The numerical evaluation of the turbulent flame speed S_T can be based either on Eq. (16), or determined as the mean inflow velocity that ensures that the flame is retained statistically stationary at a specified location. The comparison shown in Figure 11, for selected values of $\mathcal{M}$ and intensity v_c'/S_L, verifies that the two methods yield identical results (within the accuracy of the calculations). The graph shows the development of the solution in time via the control system until the flame has reached a statistically stationary state; the time average of the asymptote corresponds to the turbulent flame speed. Another way to compute the turbulent flame speed is by averaging the flame speed relation (11). Since $\overline{\psi_t} = 0$, using the definition (16) for S_T, one finds

$$S_T = \overline{\frac{\mathbf{v}^* \cdot \nabla \psi}{|\mathbf{j} \cdot \nabla \psi|}} \quad (17)$$

where the $*$ denotes evaluation at the flame front. When the flame surface is represented by a single-valued function, $\psi \equiv y - f(x, t)$, this relation simplifies to

$$S_T = \overline{u^* f_x} + \overline{v^*}$$

In general, u^* and v^* differ from their values far upstream because of the flow induced by gas expansion. For
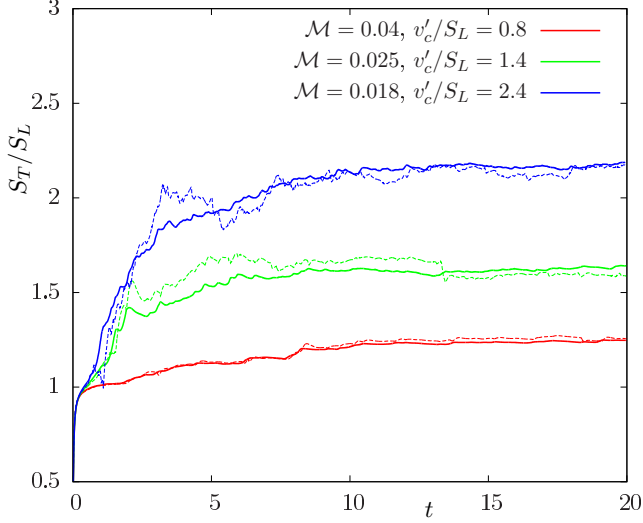
15

Figure 12: Comparison of the turbulent flame speed calculated using Eq. (16) - solid lines, and Eq. (17) - dashed lines, for selected values of the parameters. The graph shows the transient solution obtained via the control system until the flame reaches a statistically stationary state.

weakly corrugated flames, or when thermal expansion is neglected, these differences are negligible and the right hand side can be evaluated at the inflow boundary where $\mathbf{v} = (u', \overline{v} + v')$, with u', v' the velocity fluctuations which, by definition, have zero mean. Consequently $\overline{u' f_x} = 0$ since f_x and $-f_x$ are statistically identical, and $S_T = \overline{v}$, as it should. When the flame is multi-valued and highly corrugated, the flow induced by thermal expansion may be quite significant, and the right hand side of (17) cannot be approximated by the inflow conditions. It has been verified numerically that when evaluated at the flame front it is indeed equal to S_T, as shown in Fig. 12, maintaining consistency with the previous determinations of the turbulent flame speed. Here too, the graph shows the development of the solution in time via the control system until the flame has reached a statistically stationary state.

The results reported below on the turbulent flame speed span the range of turbulence intensities $v'_c/S_L \sim 0 - 2.5$. Although the hydrodynamic theory allows for arbitrary flame displacements and flow nonuniformities, it is strictly speaking valid only for weak stretch, which restricts the calculations to values of v'_c that are not too large, such that S_f remains positive everywhere and at all times. Moreover, the focus has been on two values of Markstein number $\mathcal{M} = 0.05$ and 0.033, corresponding to sub- and super-critical conditions, respectively. Results spanning a wider range of Markstein numbers will be reported in a sequel.

Figure 13(a) shows the dependence of the turbulent

flame speed normalized by the laminar flame speed S_T/S_L, on turbulence intensity v'_c/S_L. For low turbulence levels ($v'_c/S_L \lessgtr 1$) the turbulent flame speed follows a quadratic scaling with intensity of the form

$$S_T/S_L = a + b\,(v'_c/S_L)^2$$

in both the sub- and super-critical regimes (dashed curves in the figure). The constant a, which is the limiting value when $v'_c \to 0$, is related to the propagation speed of the *stable* laminar flame that results under the specified conditions, namely $a = 1$ for sub-critical conditions and $a = U_L/S_L > 1$ for super-critical conditions, where U_L is the speed of the stable cusp-like structure that results as a consequence of the DL instability. The primary reason for the increase in speed with increasing values of v'_c in this regime is the corresponding increase in flame surface area due to the augmented flame corrugations caused by the higher turbulence levels. This can be verified by noting that the mean flame area $\overline{A_f}/A$ increases in a similar quadratic fashion for both values of $\mathcal{M}$, as shown in Fig. 13(b). For subcritical conditions the increase in surface area is due to the corrugations developing on the nominally planar flame; for supercritical conditions the stable cusp-like flame which, when $v'_c = 0$ starts with a much larger surface area, is further corrugated by its interaction with turbulence at a similar rate.

At moderate values of turbulence intensity ($v'_c/S_L \gtrless 1$), the quadratic scaling is no longer valid and the turbulent flame speed follows a sub-linear scaling of the form

$$S_T/S_L \sim C(v'_c/S_L)^n$$

with exponents $n = 0.31$ and $n = 0.26$ in the sub- and super-critical regimes, respectively, as seen in Fig. 13(a) (solid curves). Such a sub-linear scaling can again be attributed to the net rate of surface area augmentation caused by the turbulence, as evident from Fig. 13(b) which shows that $\overline{A_f}/A$ varies in a *similar* sub-linear fashion. However, the exponents for the dependence of the mean flame area on turbulence intensity are much larger, $n = 0.48$ and $n = 0.39$ in the sub- and super-critical regimes, respectively, suggesting that factors other than surface area increase affect the turbulent flame speed. We will show below that the leveling in the rate of increase of the turbulent flame speed with turbulence intensity, from a quadratic to a sub-linear dependence, is due to frequent flame folding and detachment of pockets of unburned gas that cause a reduction in the average main surface area of the flame, while the lower exponents in the scaling law for S_T/S_L compared to that of $\overline{A_f}/A$ is due to flame stretch-
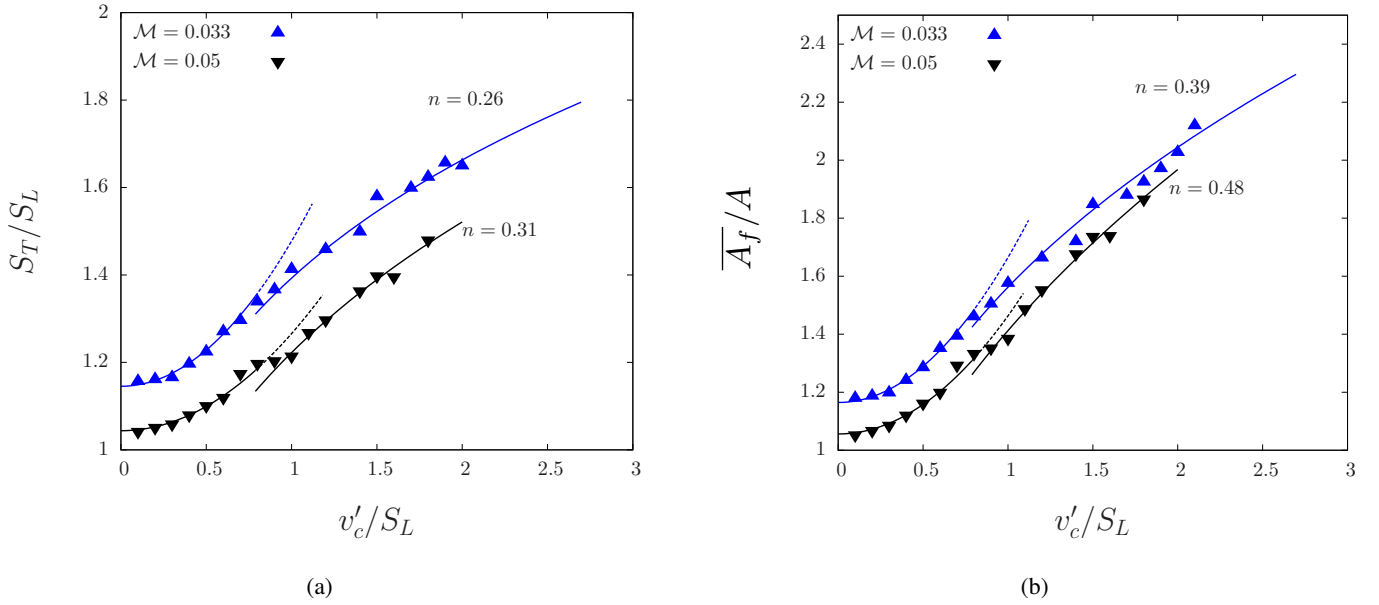
16

Figure 13: Variation of (a) the turbulent flame speed S_T/S_L, and (b) the mean flame area $\overline{A_f}/A$ with turbulence intensity v_c'/S_L for two values of the Markstein number. Also shown are quadratic fits of the form $a + b(v_c'/S_L)^2$ at low intensities (dashed lines) and sub-linear fits of the form $C(v_c'/S_L)^n$ at high intensities (solid lines).

ing.

In Fig. 14, we show snapshots of a segment of the flame surface, and the corresponding instantaneous changes in the flame surface area and speed as the flame folds and pockets of unburned gas detach from its surface, identifying various stages during this event. The instantaneous values correspond to an average taken only over the cross-sectional area of the flame segment under consideration, i.e., without averaging in time. The sequence illustrates the process of flame folding (stages A-B), pinching up pockets of unburned gas from the flame surface (C-D) and their rapid consumption (E-F). There is an increase in flame surface area, and a corresponding increase in speed when the flame folds, while the detachment and rapid consumption of pockets causes a sharp decrease in both. Such a sharp decrease in area due to pocket formation was also observed by Chen et al. [80] in their two dimensional DNS of a premixed lean methane-air flame. Such events occur frequently at high turbulence intensities, leading to a significant reduction in the rate that $\overline{A_f}/A$ increases with turbulence intensity from an ever-increasing quadratic dependence to a sub-linear scaling. A similar role in flame surface area on the turbulent flame speed was identified by Filatyev et al. [21] in their experimental study of turbulent CH_4-air flames on a slot Bunsen burner. It is also evident from the figure that the variations in average local flame speed, which differs from the laminar flame speed S_L, depends on the flame conformation and thus plays some role

in the determination of the turbulent flame speed.

To investigate this further, we calculate the average local flame speed, obtained by averaging (9) in time and over the entire flame surface, namely

$$\overline{S_f} = \lim_{\Delta t \to \infty} \frac{1}{\Delta t} \int\limits_t^{t+\Delta t} \lim_{A_f \to \infty} \left\{ \frac{1}{A_f} \iint S_f \, dA_f \right\} dt \quad (18)$$

Although the definition here differs from the "mean" introduced in (15), to avoid additional cumbersome notation we have retained the use of an "overline" to denote both (with no confusion introduced). The expression for the flame speed (10) then implies that $\overline{S_f} = S_L - \mathscr{L}\overline{\mathbb{K}}$, where $\overline{\mathbb{K}} = S_L\overline{\kappa} + \overline{K_S}$ is the mean stretch rate experienced by the turbulent flame, with $\overline{\kappa}$ the mean curvature and $\overline{K_S}$ the mean hydrodynamic strain. These are plotted in Fig. 15 as a function of turbulence intensity for $\mathcal{M} = 0.05$ (sub-) and 0.033 (super-critical conditions). For all values of v_c'/S_L the flame is, on the average, negatively curved and subjected to positive straining. The mean curvature, which is nearly zero at low intensities, is generally much smaller in magnitude than the mean strain rate. Hence, the mean stretch rate $\overline{\mathbb{K}} > 0$, or *the turbulent flame is positively stretched for all turbulence intensities*, with primary contributions to the stretch rate coming from the hydrodynamic strain. This behavior is consistent with the reported experimental measurements of Filatyev
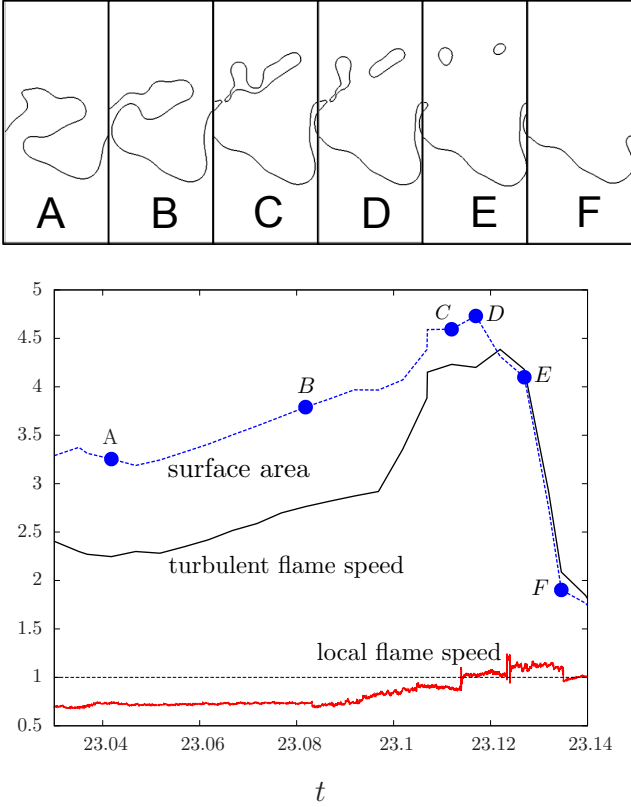
17

Figure 14: Snapshots of a segment of the flame surface (for $v_c'/S_L = 1.6$ and $\mathcal{M} = 0.05$) during the creation of pockets of unburned gas and the corresponding variations in flame surface area and speed on time, identifying the various stages during this event by the letters A-F. Also shown are the variations of the average local flame speed $\overline{S_f}/S_L$ during this time period.
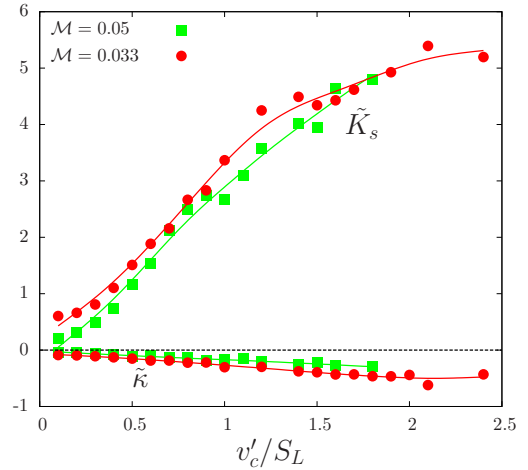

Figure 15: Variation of the dimensionless mean curvature $\tilde{\kappa} = L\overline{\kappa}$ and hydrodynamic strain rate $\tilde{K}_S = L\overline{K_s}/S_L$, with turbulence intensity v_c'/S_L; calculated for $\mathcal{M} = 0.05, 0.033$.

et al. [21] and the two-dimensional DNS of Im and Chen [37] and contrary to certain theoretical formulations [30] where the effect of scalar-strain co-variance in context of flame surface destruction has been neglected.

The mean stretch rate and local flame speed are plotted as a function of v_c'/S_L in Fig. 16, for $\mathcal{M} = 0.05, 0.033$. At low to moderate intensities, the mean stretch increases with turbulence intensity, resulting in lower values of $\overline{S_f}$, but for sufficiently high intensity values the mean stretch rate starts to level off and the mean local flame speed exhibits a bending behavior. The distinct response to the turbulence level is clearly seen in the graph for $\mathcal{M} = 0.033$ where the data below/above $v_c'/S_L \approx 1.5$ appears to fit curves of different slopes. Such leveling/bending behavior was identified by Joulin [81] in the context of a laminar stretched flame. Using a constant density model, he examined the linear response of a premixed flame to prescribed curvature and stretch and concluded that as the frequency of forcing increased beyond the reciprocal of the flame residence time $\sim l_f/S_L$, the local flame speed

becomes less and less sensitive to stretch. In their two-dimensional simulation of premixed CH_4-air and H_2-air turbulent flames, Chen and Im [82, 83] also concluded that at high turbulence intensities, as the eddy turnover time $\sim \ell/v_c'$ reduces significantly compared to the flame residence time, the flame becomes less responsive to unsteady straining. Similar conclusions were deduced in recent experiments on spherically expanding CH_4-air, C_3H_8-air and H_2-air flames [84] and on dump-stabilized axisymmetric syngas (H_2-CO blends) flames [85].

The decrease in average local flame speed $\overline{S_f}$ with increasing turbulence intensity explains the lower values of exponents in the scaling of S_T seen in Fig. 13(a) when compared to those of $\overline{A_f}/A$ seen in Fig. 13(b), and the change to a relatively slower decrease in local fame speed at higher values of v_c' explicates the bending effect exhibited by S_T.

To isolate the effects of stretching, the turbulent flame speed scaled with respect to the mean local flame speed is plotted in Fig. 17 as a function of the turbulence intensity. This entails to comparing the speed of the turbulent flame to that of a laminar flame stretched at a rate $\overline{\mathbb{K}}$, rather than a laminar unstretched planar flame. The figure clearly shows the DL enhancement of the turbulent flame speed at low turbulence intensities, for $\mathcal{M} < \mathcal{M}_c$, and the diminishing influence of the instability as v_c' increases consistent with the behavior of the flame topology and its statistics examined earlier. At low turbulence intensities ($v_c'/S_L \lessapprox 1$), the turbulent flame speed $S_T/\overline{S_f}$ follows a quadratic scaling in both the sub- and super-critical regimes. At moderate values of v_c'/S_L, different scalings
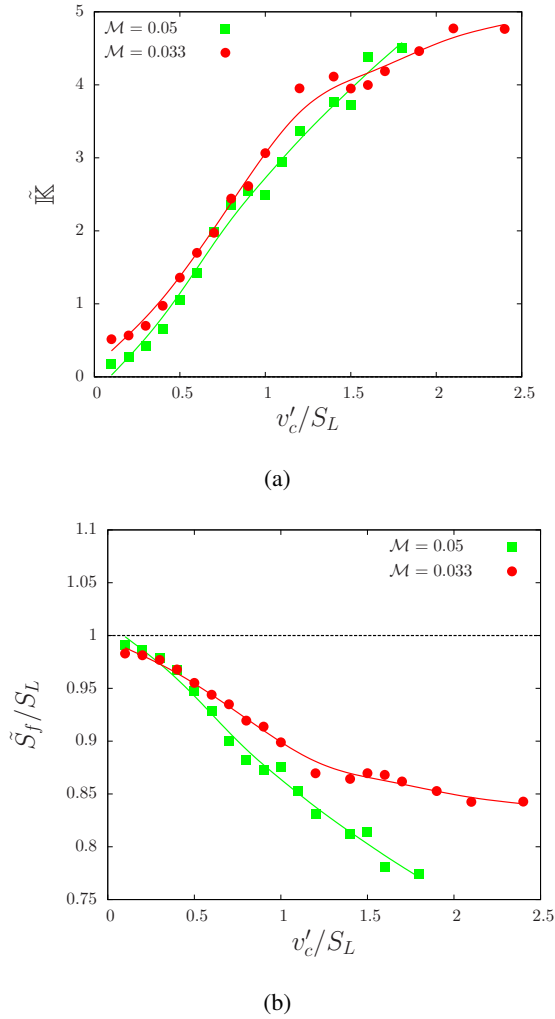
(a)

(b)

Figure 16: Variation of (a) the dimensionless mean stretch rate $\tilde{\mathbb{K}} = L\overline{\mathbb{K}}/S_L$, and (b) mean local flame speed $\overline{S_f}/S_L$ with turbulence intensity v'_c/S_L; calculated for $\mathcal{M} = 0.05, 0.033$.

emerge for the two regimes: $n = 0.51$ for sub-critical conditions and $n = 0.35$ for super-critical conditions, indicating that when the DL mechanism is active (super-critical conditions) the flame is less sensitive to the incoming turbulence. The two curves merge at $v'_c/S_L \approx 2$, which marks the transition to the highly-turbulent regime where the effects of the DL instability have been completely overshadowed by turbulence. Thereafter, the turbulent flame speed follows a single scaling law; a detailed discussion of this highly-turbulent regime will be investigated in the future. It should be noted that the transition to the highly-turbulent regime is slightly delayed when further reducing the Markstein number. Similar behavior, that we have termed *resilience to turbulence*, was previously predicted in the context of the Michelson-Sivashinsky equation, valid for weak thermal expansion [60]. The critical value, $v'_c/S_L \approx 3$ where DL influences
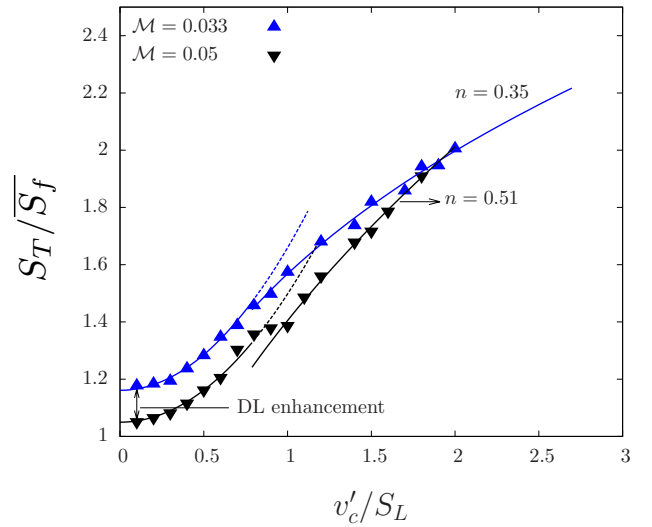

Figure 17: Variation of the turbulent flame speed scaled with the mean local flame speed $S_T/\overline{S_f}$ with turbulence intensity v'_c/S_L for two values of the Markstein number. Also shown are quadratic fits of the form $a + b(v'_c/S_L)^2$ at low intensities (dashed lines) and sub-linear fits of the form $C(v'_c/S_L)^n$ at high intensities (solid lines).

cease to be significant, that has been estimated in [26] based on their experimental data of spherically expanding turbulent C_8H_{18}-air flames is within the range of our predictions; the slightly larger value could be a result of a smaller Markstein number due either to the mixture composition ($\phi = 1.4$) or the system pressure (2 MPa). The existence of two different scaling laws for S_T due to instability effects that merge to one when the DL effects are weakened was reported in [30], and in the recent experimental study of C_3H_8-air turbulent Bunsen flames [28].

Figure 17 also shows that the dependence of the turbulent flame speed, with the effects of stretching scaled out, is in close agreement with the dependence of the area ratio of Fig. 13(b) on turbulence intensity. The exponents of the curve fit are also nearly equal to the exponents of the scaling of $\overline{A_f}/A$, for both sub- and supercritical conditions. This suggests that $S_T/\overline{S_f} \approx \overline{A_f}/A$, or

$$S_T = \overline{S_f \frac{|\nabla\psi|}{|\mathbf{j} \cdot \nabla\psi|}} \approx \overline{S_f} \cdot \overline{\frac{|\nabla\psi|}{|\mathbf{j} \cdot \nabla\psi|}} \qquad (19)$$

implying that the stretch rate is effectively statistically independent of the flame surface area. Their correlation, shown in Fig. 18 as a function of v'_c/S_L for selected values of Markstein number, is indeed small for the turbulence levels considered, noting that it may become significant at higher turbulence intensities. A similar observation about the statistical independence of the strain rate experienced by the flame and its surface area was made by Peters [43]
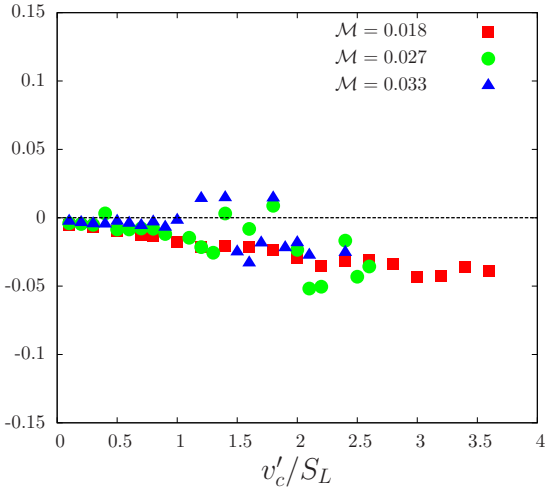
19

Figure 18: The correlation coefficient $\overline{S_f\,(|\nabla\psi|/|\mathbf{j}\cdot\nabla\psi|)}\, - \,\overline{S_f}\,(\overline{|\nabla\psi|/|\mathbf{j}\cdot\nabla\psi|})$ plotted as a function of the turbulence intensity v_c'/S_L for representative values of Markstein number.

based on a constant-density model in the context of the G-equation.

Based on the above considerations the following scaling laws are proposed. For low turbulence intensities ($v_c'/S_L \lesssim 1$),

$$\frac{S_T}{S_L} = \left(1 - \frac{\mathscr{L}\overline{\mathbb{K}}}{S_L}\right)\left[a + b\left(\frac{v_c'}{S_L}\right)^2\right] \qquad (20)$$

where

$$a = \begin{cases} 1 & \text{for } \mathcal{M} > \mathcal{M}_c \\ U_L/S_L & \text{for } \mathcal{M} < \mathcal{M}_c \end{cases}$$

Such quadratic scaling was reported[2] in our earlier publications [46, 61] where, in addition, the dependence of the coefficient b on Markstein length, thermal expansion and turbulence integral scale has been delineated. It is also in agreement with the rigorous perturbation study of Clavin and Williams [6], and with the heuristic suggestions of Damköhler [4] and Shelkin [5]. For moderate-to-high turbulence intensities ($v_c'/S_L \gtrsim 1$),

$$\frac{S_T}{S_L} = C\left(1 - \frac{\mathscr{L}\overline{\mathbb{K}}}{S_L}\right)\left(\frac{v_c'}{S_L}\right)^n \qquad (21)$$

with

$$n \approx \begin{cases} 0.51 & \text{for } \mathcal{M} > \mathcal{M}_c \\ 0.35 & \text{for } \mathcal{M} < \mathcal{M}_c \end{cases} \qquad (22)$$

The functional dependence of the coefficient C on the system parameters will be reported in a sequel. The turbulent flame speed may also be expressed as

$$\frac{S_T}{S_L} = \left(1 - \frac{\mathscr{L}\overline{\mathbb{K}}}{S_L}\right)\overline{\frac{A_f}{A}}$$

where the area ratio $\overline{A_f/A}$ follows a quadratic scaling at low intensities and sub-linear scaling $\sim (v_c'/S_L)^n$ at higher intensities, with exponents n given approximately by (22).

Measured values of the turbulent flame speed obtained from various experimental studies reported by Lipatnikov and Chomiak [2, Section 3.3.1] and from the recent studies [28, 86] were found to obey a scaling law of the form (21) with exponent $n \approx 0.4 - 0.5$. These results are in better agreement with our scaling law for the area ratio $\overline{A_f/A}$ and not with the scaling law for the turbulent flame speed S_T/S_L. The reason lies in the common practice in experimental studies to multiply the area of various segments comprising the flame surface by the laminar flame speed S_L instead of the local flame speed S_f, which leads to predictions that do not account for the effects of flame stretch. Our results indicate that not accounting for the stretching factor would result in an over-estimation of the turbulent flame speed by nearly 10 - 15%. It should be noted that some recent studies [84, 85, 87] have attempted to experimentally quantify this factor.

Indeed, the significance of the stretch rate on turbulent flame propagation has been previously recognized. In modeling the mean reaction rate in the averaged energy and species governing equations Bray [12] introduced a stretch factor, which was later estimated from the asymptotic relation (10), as discussed in [88, 89] or via numerical simulations, as discussed in [3]. In our result the stretch factor is a consequence of the simulations and its form is a direct result of the local flame speed relation (10) adopted in the hydrodynamic model. It should be emphasized that introducing a multiplicative stretch factor remains valid as long as the flame surface area and the stretch rate it experiences are statistically independent, as commented above.

5. Flame-turbulence interactions

The effect of the flame on the turbulent flow field is best illustrated by examining the evolution of the vorticity $\boldsymbol{\omega}$,

---

[2]In the referenced papers the turbulent flame speed for supercritical conditions has been normalized by U_L, such that S_T for different values of $\mathcal{M}$ tend to the same limit as $v_c' \to 0$.

described by the equation

$$\frac{D\boldsymbol{\omega}}{Dt} = (\boldsymbol{\omega}\cdot\nabla)\mathbf{v} - \boldsymbol{\omega}(\nabla\cdot\mathbf{v})$$
$$+ \frac{1}{\rho^2}(\nabla\rho\times\nabla p) + \nabla\times\left(\frac{1}{\rho}\nabla\cdot\mu\boldsymbol{\Sigma}\right). \quad (23)$$

The first and third terms on the right hand side correspond, respectively, to vorticity generation due to vortex stretching, which is absent in the two-dimensional flow considered here, and through the baroclinic torque mechanism caused by the misalignment of the density gradient (normal to the flame surface) and the local pressure gradient. The second and fourth terms on the right hand side of (23) correspond, respectively, to vorticity destruction by volumetric expansion, whereby the vorticity in the burned gas region is spread over a greater volume, and by viscous diffusion (of little significance near the flame). In the present context, the most significant contributions are the destruction of vorticity due to volumetric expansion and its production through the baroclinic torque mechanism. Creta and Matalon [46] have shown that under sub-critical conditions the destruction of vorticity via volumetric expansion is the dominant effect, because the fluctuating flames are nearly flat and the baroclinic torque mechanism is ineffective. Under super-critical conditions, however, both effects are active, with the baroclinic production of vorticity playing an increasing role as the Markstein number is continuously decreased below criticality, as discussed below.

Figure 19 shows the mean value (in time and in transverse direction) of the magnitude of vorticity $\overline{|\omega|}$, suitably rescaled with its value $\overline{|\omega_1|}$ far upstream, for turbulent flames corresponding to two values of the Markstein number. For sub-critical conditions, $\mathcal{M} = 0.057$, the destruction of the incident vorticity by volumetric expansion is evident for all values of v_c'. The average value of the vorticity in the burned gas, however, increases with increasing turbulence intensity; due to the shorter flow time scale the vortices pass through the flame with minor attenuation. For super-critical conditions, $\mathcal{M} = 0.018$, the accentuated vorticity in the burned gas at low turbulence intensity is a result of the elevated vorticity production near the cusp region of the DL flame conformation. The decrease in vorticity level with increasing turbulence intensity, up to $v_c'/S_L = 2.4$ say, is due to the diminishing influence of the DL instability. As the turbulence intensity increases further, the vorticity level across the burned gas region starts to increase due to reduced attenuation of vortices with shorter timescales, similar to our observation in the sub-critical case, and consistent with the nature of
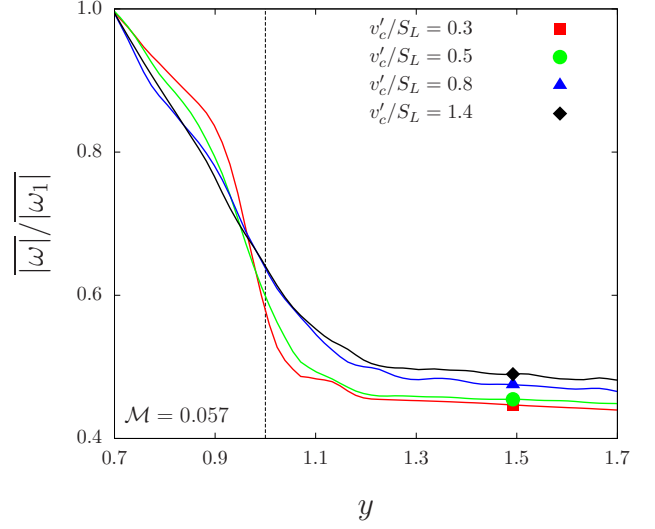
(a) Sub-critical conditions, $\mathcal{M} = 0.057$
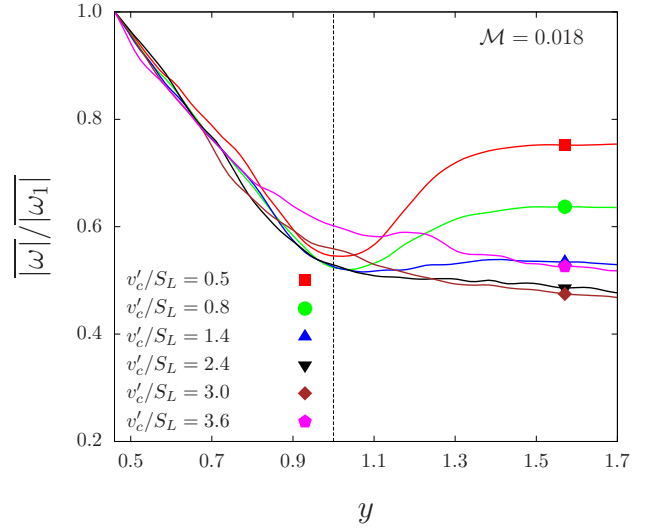
(b) Super-critical conditions, $\mathcal{M} = 0.018$

Figure 19: Mean vorticity, scaled relative to its upstream value, across turbulent flames, parametrized with increasing values of v_c'/S_L; the mean location of the flame is held at $y = 1$, marked by the vertical line.

the flame in the highly-turbulent regime, where the flame is dominated by the turbulence. A similar observation regarding the vorticity suppression by volumetric expansion was made by Hamlington et al. [90] based on their three-dimensional DNS study of H_2-air turbulent flames over a wide range of turbulence intensities $v_c'/S_L = 2.45 - 30.6$; a reduction in vorticity suppression, or a relative increase in vorticity level in the burned gas region, was noted when increasing the turbulence intensity.

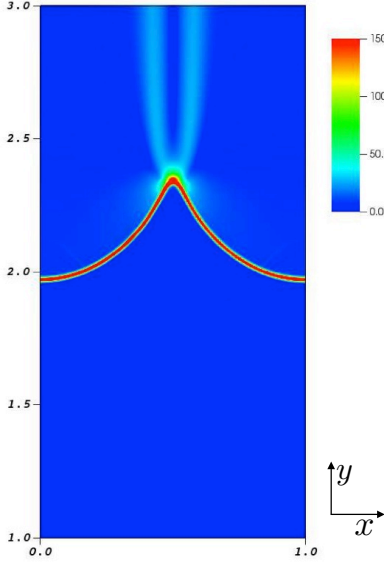Another characteristic that demonstrates the flame-turbulence interaction is the strain rate field $E =$

Figure 20: Strain rate field across a stable laminar cusp flame; calculated for $\sigma = 5$ and $\mathcal{M} = 0.018$.

$(e_{ij}e_{ij})^{1/2}$. Neglecting viscous effects (which play an insignificant role in our model), the evolution equation (in indicial notation)

$$\frac{De_{ij}}{Dt} = -e_{ik}e_{kj} - \frac{1}{4}(\omega_i\omega_j - \delta_{ij}\omega_k\omega_k) - \frac{1}{\rho}\frac{\partial^2 p}{\partial x_i \partial x_j}$$
$$+ \frac{1}{2\rho^2}\left(\frac{\partial p}{\partial x_i}\frac{\partial \rho}{\partial x_j} + \frac{\partial p}{\partial x_j}\frac{\partial \rho}{\partial x_i}\right), \quad (24)$$

obtained by differentiating the momentum equations (13b), shows that both the density gradients as well as the vorticity field across the flame are the main contributions to the production of the strain. This is clearly illustrated in Fig. 20 which shows that the strain field of a cusped-shape laminar flame bears a striking resemblance of the vorticity field shown in Fig. 6. The region along the flame surface is highly strained due to the large density gradient and vorticity production, with substantial strain originating near the highly curved cusp, where vorticity is generated via the baroclinic torque mechanism and convected downstream.

In Fig. 21 we show the mean value of the strain rate field $\overline{E}$ (in time and transverse direction), suitably rescaled with respect to its value $\overline{E_1}$ far upstream, for turbulent flames corresponding to two values of the Markstein number. It should be noted that the figure displays the vertical variations of the mean strain rate, different from the mean strain rate $\overline{K_S}$ experienced by the flame, which is measured along the flame surface. For both values of $\mathcal{M}$, the mean strain is most significant in the region spanned by the flame brush as a result of gas expansion and peaks near the flame surface. As the turbulence
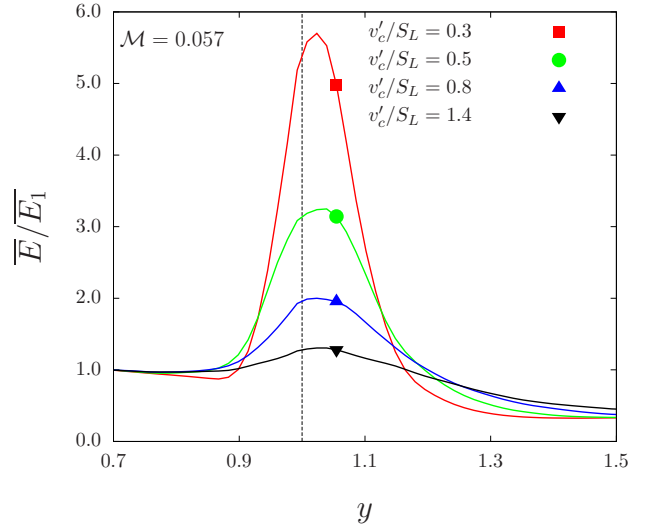
(a) Sub-critical conditions, $\mathcal{M} = 0.057$
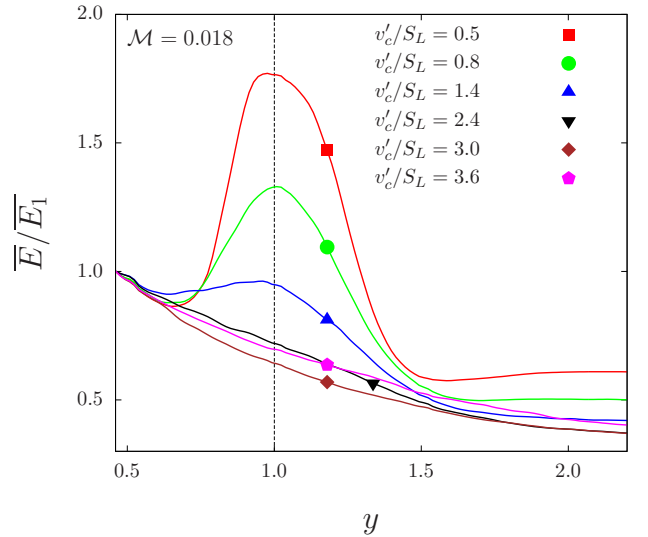
(b) Super-critical conditions, $\mathcal{M} = 0.018$

Figure 21: Mean strain, scaled relative to its upstream value, of turbulent flames parametrized with increasing values of v'_c/S_L. The mean location of the flame is held at $y = 1$, marked by the vertical line.

intensity increases, the mean strain spreads over a wider vertical region spanned by the flame brush, causing a decrease in the overall level of $\overline{E}$ near the flame. The behavior in the burned gas region, however, is different for the two Markstein numbers. For sub-critical conditions, $\mathcal{M} = 0.057$, the mean strain continuously decays beyond the flame, but attains larger values for larger values of v'_c. For super-critical conditions, $\mathcal{M} = 0.018$, substantial strain is present downstream of the flame region at low turbulence intensities, namely when the flame is strongly

affected by the DL instability. The additional strain diminishes when v'_c further increases, but at sufficiently high intensities the mean strain distribution becomes again similar to the one observed for sub-critical conditions. Similar trends to those observed for sub-critical conditions were reported by Hamlington et al. [90]. They decompose $\overline{E}$ into a flame contribution $\overline{E}_f$, which embodies effects of fluid expansion, and a turbulence contribution $\overline{E}_T$, and show a decrease in $\overline{E}_f$ and an increase in $\overline{E}_T$ with increasing turbulence intensity. Our results extend this discussion by showing that when DL influences are significant, i.e., for supercritical conditions, $\overline{E}_f$ contains an additional contribution due to the vorticity generation via the baroclinic mechanism near the sharp flame crests.

6. Conclusions

In this paper we have systematically characterized the topology and dynamics of turbulent premixed flames within the context of an asymptotic hydrodynamic model. The flame, represented as a surface separating burned from unburned gases with different densities and temperatures, propagates relative to the fresh mixture at a speed that depends on the local stretch rate, modulated by a Markstein length $\mathscr{L}$ that mimics the influences of diffusion and chemical reactions occurring inside the flame zone. The propagation is therefore affected by the local mixture composition and flow conditions, and the flow field is modified in turn by the gas expansion resulting from the combustion process. Implicit in this description is the assumption that the small turbulent eddies do not modify the preheat and reaction zones which retain their laminar structure with transport and chemistry accounted for through the Markstein length. The values of Marsketein length, the range of turbulence intensities and the integral scale considered in this work place the results in the wrinkled-to-corrugated regimes of turbulent combustion.

We show the existence of different flame response to low, moderate, and high turbulence intensities and to different values of the Markstein length. The various flame behaviors have been properly delineated by numerous statistical properties of the turbulent flame, including the p.d.f.'s of the flame position and curvature, the skewness of the curvature, the cross correlation between curvature and strain, and the effect of the flame on the incident flow. We conclude:

1. At low turbulence intensity, $v'_c/S_L \lessapprox 1$, two modes of propagation exist depending on whether the

Darrieus-Landau (DL) instability has an influence on the flame propagation. For sub-critical conditions, corresponding to a Markstein number $\mathcal{M} > \mathcal{M}_c$, the fluctuating turbulent flame is unaffected by the instability and remains "planar" on the average. In contrast, for super-critical conditions corresponding to a Markstein number $\mathcal{M} < \mathcal{M}_c$, the turbulent flame experiences frequent sharp intrusions into the burned gas region, leading to thicker flame brushes whose dynamics is partially resilient to the turbulence. The terms sub- and super-critical are borrowed from the analogous flame behavior under laminar conditions, where the onset of the DL instability is a bifurcative phenomenon and the critical Markstein number is uniquely determined by Eq. (14). In the turbulent case the transition occurs gradually; when conditions come near criticality the properties of the "planar" flame brush are progressively modulated by the instability [61]. In both cases, the increase in speed of the turbulent flame depends quadratically on the turbulence intensity but, whereas for sub-critical conditions the nominal flame is planar and the increase in speed due to the turbulence augments the laminar flame speed S_L, the nominal flame for supercritical condition is the much faster propagating cusped-shape flame and the increase in speed due to the turbulence augments the propagation speed $U_L > S_L$.

2. The distinct flame behavior for sub- and super-critical conditions remains notable at moderate turbulence intensities ($1 \lessapprox v'_c/S_L \lessapprox 2$) insofar as their turbulent propagation speed is concerned, with super-critical flames propagating faster than sub-critical flames. However, the strong influence of the DL instability for super-critical conditions progressively diminishes and the distinct shape of the flame brush that characterizes this mode of propagation becomes less visible. Of greater significance is the dependence of the turbulent flame speed on turbulence intensity, which varies from a quadratic to a sub-linear scaling, suggesting that other factors impeding on the increase in flame surface area affect the turbulent flame speed. The extent of this transitional regime or, equivalently, the range of influence of the DL instability depends on the Markstein length, with the more unstable flames (i.e., corresponding to lower values of the Markstein number $\mathcal{M}$) retaining their distinct characteristics to larger values of v'_c/S_L.

3. At high turbulence intensity, $v'_c/S_L \gtrapprox 2$, the flame is dominated completely by the turbulence and the

influences of the DL instability play limited to no role on its propagation. The flame brush for sub- and super-critical conditions is indistinguishable, and the associated p.d.f.s tend towards symmetric and nearly identical shapes. The exact dependence of the turbulent flame speed on turbulence intensity, which appears to become independent of the Markstein length, remains to be determined.

The aforementioned conclusions clearly identifies the role of the DL instability on premixed turbulent flames, in mixtures corresponding to $\mathcal{M} < \mathcal{M}_c$, causing an enhancement in speed at low turbulence levels that gradually diminishes at higher intensities, as the flame becomes increasingly controlled by the turbulence. Our results also show that the dependence of the turbulent flame speed on turbulence intensity exhibits a *bending* trend, whereby the nearly quadratic dependence at low turbulence levels transitions to a sub-linear scaling at high turbulence intensities. The increase in speed with increasing turbulence intensity is primarily due to the increase in the flame surface area, as envisioned by the pioneering work of Damköher. The leveling in the rate of increase of the turbulent flame speed with turbulence intensity is partially due to the frequent folding of the flame surface, which results from the more vigorous turbulence, leading to the detachment of pockets of unburned gas that are rapidly consumed and a reduction in the main surface area of the flame. Another effect that leads to the reduction in speed is the fact that the convoluted flame is highly stretched, which leads to a reduction in the local propagation speed, as appropriate for mixtures of positive Markstein length, and consequently a reduction in the turbulent flame speed. From our results, we observe that flame stretching results in a reduction of the turbulent flame speed by $10 - 15\%$ for $v'_c/S_L \gtrsim 1$, and contrary to the often stated belief, is almost entirely due to hydrodynamic straining with curvature contributing less that 15% to the mean stretch rate.

The novelty of our results is in expressions (20)-(21) for the turbulent flame speed, which exhibit explicit dependencies on the turbulent intensity and mean stretch rate experienced by the flame, and on physically measurable quantities through the coefficient C; the dependence of the coefficient C on thermal expansion, Markstein length and integral scale was discussed for low values of v'_c/S_L in [61] and will be presented for higher turbulence intensities in a sequel. Moreover, these results were deduced from physical first principles, without invoking any turbulence modeling assumptions or introducing adjustable parameters. Admittedly, with the flame confined to a sur-

face, possible modifications of its internal structure by the turbulence have been neglected. Nevertheless, effects due its finite thickness have been accounted for through the Markstein length. For example, an increase in the system pressure results in a thinner flame and, consequently, in a lower Markstein length $\mathscr{L}$. For low turbulence intensity under super-critical conditions, it was found [46] that the coefficient $C \sim \mathcal{M}^{-m}$, with $m \approx 0.4$, implying that the turbulent flame speed $S_T \sim P^m$, in accord with the experimental results of Kobayashi et al. [91].

Our results further indicate that the turbulent flame speed, when scaled with the laminar flame speed, takes the form $S_T/S_L = (\overline{S_f}/S_L)(\overline{A_f}/A)$, namely the product of two factors; the relative drop in local flame speed as a result of stretching and the relative increase in flame surface area as a result of turbulence. A common practice in experimental studies is to determine the turbulent flame speed by accounting for the increase in flame surface only, effectively neglecting the effects of stretch. Numerous such studies have reported scaling laws for the turbulent flame speed $\sim (v'_c/S_L)^n$ with exponent $n \approx 0.4 - 0.5$ similar to our scaling of the mean flame area $\overline{A_f}/A$ for moderate-to-high turbulence intensities. This practice results in an over-estimation of the turbulent flame speed, which when accounting for stretch effects will result with an exponent $n \approx 0.25 - 0.3$.

Our results are limited to mixtures with Markstein length $\mathscr{L} > 0$, such as lean hydrocarbon-air or rich hydrogen-air mixtures, where thermo-diffusive effects have a stabilizing influence on the flame. A recent DNS study [62] of hydrodynamically-unstable corrugated (laminar) flames in H_2-air mixtures showed that thermo-diffusive instabilities start affecting the flame surface only at equivalence ratios below $\phi \approx 0.7$, and that the predictions of the hydrodynamic model for the richer flames agree extremely well with the simulations. The development of small scale perturbations on the flame surface for leaner flames lead to a substantial increase in propagation speed, which is not captured by the asymptotic model. A similar increase in speed is anticipated for turbulent flames for mixtures with $\mathscr{L} < 0$.

Appendix A

The evolution and deformation of the flame surface, which is represented by the zero level of the function $\psi(x, y, t)$, is described by the partial differential equation (11). Numerically this equation is solved on a rectangular grid, requiring algorithms (i) to reconstruct the implicit surface from the scattered data, in order to properly eval-
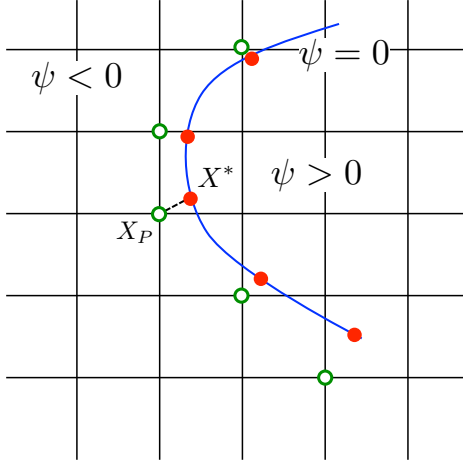
24

Figure 22: Illustration of irregular points (in green/open circles) on the Cartesian grid, used for the reconstruction process and Lagrangian points on the zero level curve ($\psi = 0$) (in red/closed circles), obtained via the projection of irregular points on to the zero level in the direction of the normal (dashed line) to the zero level surface. Also marked is an example irregular point X_p and its corresponding Lagrangian point X^*.
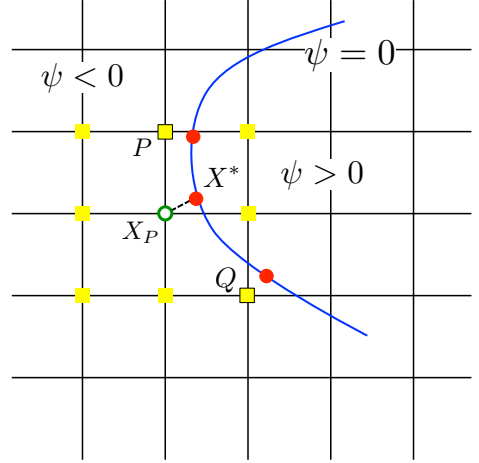

Figure 23: An illustration of a projection point $\mathbf{X_p}$ (in green/open circles), associated with the zero point $\mathbf{X}^*$ (in red/filled circles) on the level surface and its neighbors (in yellow/filled squares) on the Cartesian grid.

uate the velocity field $\mathbf{v}^*$ used to advect the flame surface, and (ii) to order the data set along the reconstructed surface, which is needed for evaluating the tangential component of the hydrodynamic strain rate K_s^{t}.

Reconstruction of the zero level set

The reconstruction of the zero level of $\psi(x, y, t)$ is performed based on the algorithm described in [92]. The main steps of the algorithm are described below, in conjunction with Fig. 22.

1. Locate an irregular grid point $\mathbf{X_p}$ on the level set function ψ, defined as a point, (x_i, y_j) say, where $\psi_{i,j} < 0$ and any one of the four neighboring points $\psi_{i+1,j}, \psi_{i-1,j}, \psi_{i,j+1}, \psi_{i,j-1} > 0$.

2. Find the steepest ascent direction $\mathbf{n} = \nabla\psi/|\nabla\psi|$ at the point X_p.

3. Project $\mathbf{X_p}$ on the zero level surface along the normal $\mathbf{n}$, locating the point

$$\mathbf{X}^* = \mathbf{X_p} + \alpha\mathbf{n}$$

where α is the solution of $\psi(\mathbf{X}^*) = 0$, approximated using a Taylor expansion by the quadratic equation

$$\psi(\mathbf{X_p}) + |\nabla\psi|\,\alpha + \frac{1}{2}(\mathbf{n}^T\!\cdot\!\mathbf{He}(\psi)\!\cdot\!\mathbf{n})\,\alpha^2 = 0\,,$$

where $|\nabla\psi|$ and the Hessian matrix of ψ

$$\mathbf{He}(\psi) = \left[\begin{array}{cc} \psi_{xx} & \psi_{xy} \\ \psi_{yx} & \psi_{yy} \end{array}\right]$$

are evaluated at $\mathbf{X_p}$.

Reordering of points along the zero level

In calculating the tangential component of the hydrodynamic strain K_S^{t}, the velocity gradient $\partial v_\tau^*/\partial s$ needs to be evaluated, where s is measured along the arc length. This requires ordering the points on the interface in a consecutive way. In the following description, which is based on the illustration shown in Fig. 23, points on the zero level surface, such as $\mathbf{X}^*$, are referred to Lagrangian points and the corresponding grid points from which the projection is made, such as $\mathbf{X_p}$, are projection points. The main steps of the algorithm are:-

1. Identify a Lagrangian point along the flame surface. Such a point $\mathbf{X}^*$ originates from a unique projection point, $\mathbf{X_p}$, since each grid point is visited only once during the reconstruction process. Once a Lagrangian point is identified, the next point must have a projection point from among the eight neighboring points of $\mathbf{X_p}$, marked in yellow/filled squares in the figure. But only those marked as $\mathbf{P}$ and $\mathbf{Q}$ are relevant, because two of them are on the wrong side of $\psi = 0$ and the others cannot be projected onto the zero level surface. If a valid projection point cannot be found within these eight neighboring points, the search is widened to $i \pm 2, j \pm 2$.

25

2. Determine the adjacent Lagrangian point according to the selected direction, and ignore points which are in the opposite direction. Assuming we move in the counter-clockwise direction, such that $\psi < 0$ is always on the interior, the next valid projection point is P. It is determined by comparing the cross products $\overrightarrow{X_pX^*} \times \overrightarrow{X_pP}$ and $\overrightarrow{X_pX^*} \times \overrightarrow{X_pQ}$; only one of these two will be positive.

3. Use the the distance from the current Lagrangian point as the elimination criteria, in case there are multiple projection points with the right sign of the above mentioned cross product, and select the point with the minimum distance as the next Lagrangian point.

This algorithm has been tested for complex shapes and was found to work well. The only drawback is that in areas of very sharp curvature, the algorithm tends to skip a few points, but that does not affect the purpose for which this algorithm is devised.

Acknowledgments

References

[1] R. G. Abdel-Gayed, D. Bradley, M. Lawes, Proc. R. Soc. Lond. A 414 (1987) 389–413.

[2] A. Lipatnikov, J. Chomiak, Prog. Energ. Combust. 28 (2002) 1–74.

[3] J. F. Driscoll, Prog. Energ. Combust. 34 (2008) 91–134.

[4] G. Damköhler, Z. Elektrochem. 46 (1940) 601–652.

[5] K. I. Shelkin, NACA TM 1110 (1947).

[6] P. Clavin, F. A. Williams, J. Fluid Mech. 90 (1979) 589–604.

[7] J. R. Mayo, A. R. Kerstein, Phys. Letters A 372 (2007) 5–11.

[8] J. R. Mayo, A. R. Kerstein, Phys. Rev. E 78 (2008) 056307 (1–18).

[9] A. Kerstein, Proc. Combust. Inst. 21 (1988) 1281–1289.

[10] V. Yakhot, Combust. Sci. Technol. 60 (1988) 191–214.

[11] G. Sivashinsky, Combust. Sci. Technol. 62 (1988) 77–96.

[12] K. Bray, Proc. R. Soc. Lond. A 431 (1990) 315–335.

[13] J. Duclos, D. Veynante, T. Poinsot, Combust. Flame 95 (1993) 101–117.

[14] H.-P. Schmid, P. Habisreuther, W. Leuckel, Combust. Flame 113 (1998) 79–91.

[15] N. Peters, J. Fluid Mech. 384 (1999) 107–132.

[16] H. Kolla, J. W. Rogerson, N. Swaminathan, Combust. Sci. Technol. 182 (2010) 284–308.

[17] D. R. Ballal, A. H. Lefebvre, Acta Astronaut. 1 (1974) 471–483.

[18] K. . Smith, F. C. Gouldin, AIAA Journal 17 (1979) 1243–1250.

[19] H. Kobayashi, Y. Kawabata, K. Maruta, Proc. Combust. Inst. 27 (1998) 941 – 948.

[20] S. S. Shy, W. J. Lin, K. Z. Peng, Proc. Combust. Inst. 28 (2000) 561–568.

[21] S. Filatyev, J. Driscoll, C. Carter, J. Donbar, Combust. Flame 141 (2005) 1–21.

[22] D. Bradley, M. Lawes, K. Liu, M. S. Mansour, Proc. Combust. Inst. 34 (2013) 1519 – 1526.

[23] G. Darrieus, Propagation d'un front de flamme, 1938. *Unpublished work*; presented at La Technique Moderne (Paris) and in 1945 at Congrès de Mécanique Appliquée (Paris).

[24] L. Landau, Acta Physicochimica USSR 19 (1944) 77–85.

[25] R. Paul, K. Bray, Proc. Combust. Inst. 26 (1996) 259 – 266.

[26] A. Al-Shahrany, D. Bradley, M. Lawes, K. Liu, R. Woolley, Combust. Sci. Tech. 178 (2006) 1771–1802.

[27] V. R. Savarianandam, C. J. Lawn, Combust. Flame 146 (2006) 1–18.

[28] G. Troiani, F. Creta, M. Matalon, Proc. Combust. Inst. 35 (2015) 1451 – 1459.

[29] V. Akkerman, V. Bychkov, Combust. Theor. Model. 9 (2005) 323–351.

[30] S. Chaudhuri, V. Akkerman, C. K. Law, Phys. Rev. E 84 (2011) 026322.

[31] H. Boughanem, A. Trouvé, Proc. Combust. Inst. 27 (1998) 971–978.

[32] J. B. Bell, M. S. Day, J. F. Grcar, Proc. Combust. Inst. 29 (2002) 1987–1993.

[33] A. J. Aspden, J. B. Bell, M. S. Day, S. E. Woosley, M. Zingale, ApJ 689 (2008) 1173–1185.

[34] A. Y. Poludnenko, E. S. Oran, Combust. Flame 157 (2010) 995–1011.

[35] A. Y. Poludnenko, E. S. Oran, Combust. Flame 158 (2011) 301–326.

[36] M. Baum, T. J. Poinsot, D. C. Haworth, N. Darabiha, J. Fluid Mech. 281 (1994) 1–32.

[37] H. G. Im, J. H. Chen, Combust. Flame 131 (2002) 246–258.

[38] J. B. Bell, R. K. Cheng, M. S. Day, I. G. Shepherd, Proc. Combust. Inst. 31 (2007) 1309–1317.

[39] M. Matalon, B. Matkowsky, J. Fluid Mech. 128 (1982) 239–259.

[40] M. Matalon, C. Cui, J. Bechtold, J. Fluid Mech. 487 (2003) 179–210.

[41] G. Giannakopoulos, A. Gatzoulis, C. Frouzakis, M. Matalon, A. Tomboulides, Combust. Flame 162 (2015) 1249–1264.

[42] R. Borghi, in: Recent Adv in the Aerosp Sci, Plenum, 1985, pp. 117–138.

[43] N. Peters, Turbulent Combustion, Cambridge, 2000.

[44] I. G. Shepherd, R. K. Cheng, T. Plessing, C. Kortschik, N. Peters, Proc. Combust. Inst. 29 (2002) 1833–1840.

[45] M. J. Dunn, A. R. Masri, R. W. Bilger, Combust. Flame 151 (2007) 46–60.

[46] F. Creta, M. Matalon, J. Fluid Mech. 680 (2011) 225–264.

[47] Y. Liu, J. Xin, Y. Yu, Phys. D (2012).

[48] F. Van der Bos, V. Gravemeier, J. Comput. Phys. 228 (2009) 3605–3624.

[49] C. Rhee, L. Talbot, J. Sethian, J. Fluid Mech. 300 (1995) 87–115.

[50] V. Smiljanovski, V. Moser, R. Klein, Combust. Theor. Model. 1 (1997) 183–215.

[51] K. Pan, W. Shyy, C. Law, Int. J. Heat Mass Transfer 45 (2002) 3503–3516.

[52] A. R. Kerstein, W. Ashurst, F. A. Williams, Phys. Rev. A 37 (1988) 2728–2731.

[53] N. Peters, J. Fluid Mech. 242 (1992) 611–629.

[54] H. Pitsch, L. Duchamp De Lageneste, Proc. Combust. Inst. 29 (2002) 2001–2008.

[55] H. Pitsch, Combust. Flame 143 (2005) 587–598.

[56] A. Almgren, J. Bell, P. Colella, L. Howell, M. Welcome, J. Comp. Phys. 142 (1998) 1–46.

[57] S. Yoo, D. S. Stewart, Combust. Theor. Model. 9 (2005) 219–254.

[58] Y. Rastigejev, M. Matalon, Combust. Theor. Model. 10 (2006) 459–481.

[59] F. Creta, M. Matalon, Proc. Combust. Inst. 33 (2011) 1087–1094.

[60] F. Creta, N. Fogla, M. Matalon, Combust. Theor. Model. 15 (2011) 267–298.

[61] N. Fogla, F. Creta, M. Matalon, Proc. Combust. Inst. 34 (2013) 1509–1517.

[62] C. E. Frouzakis, N. Fogla, A. G. Tomboulides, C. Altantzis, M. Matalon, Proc. Combust. Inst. 35 (2015) 1087 – 1095.

[63] T. W. Lee, G. L. North, D. A. Santavicca, Combust. Flame 93 (1993) 445–456.

[64] M. Z. Haq, C. G. W. Sheppard, R. Woolley, D. A. Greenhalgh, R. D. Lockett, Combust. Flame 131 (2002) 1–15.

[65] T. C. Treurniet, F. T. M. Nieuwstadt, B. J. Boersma, J. Fluid Mech. 565 (2006) 25–62.

[66] T. Echekki, J. H. Chen, Combust. Flame 106 (1996) 184–202.

[67] C. J. Rutland, A. Trouvé, Combust. Flame 94 (1993) 41–57.

[68] A. M. Steinberg, J. F. Driscoll, S. L. Ceccio, Proc. Combust. Inst. 32 (2009) 1713–1721.

[69] C. J. Mueller, J. F. Driscoll, D. L. Reuss, M. C. Drake, M. E. Rosalik, Combust. Flame 112 (1998) 342–358.

[70] J. O. Sinibaldi, C. J. Mueller, A. E. Tulkki, J. F. Driscoll, AIAA Journal 36 (1998) 1432–1438.

[71] C. Meneveau, T. Poinsot, Combust. Flame 86 (1991) 311–332.

[72] O. Colin, F. Ducros, D. Veynante, T. Poinsot, Phys. Fluids 12 (2000) 1843.

[73] F. Charlette, C. Meneveau, D. Veynante, Combust. Flame 131 (2002) 159–180.

[74] Y. Rastigejev, M. Matalon, J. Fluid Mech. 554 (2006) 371–392.

[75] A. M. Steinberg, J. F. Driscoll, Combust. Flame 156 (2009) 2285–2306.

[76] D. Haworth, T. Poinsot, J. Fluid Mech. 244 (1992) 405–436.

[77] N. Chakraborty, S. Cant, Combust. Flame 137 (2004) 129–147.

[78] B. Renou, A. Boukhalfa, D. Puechberty, M. Trinité, Proc. Combust. Inst. 27 (1998) 841–847.

[79] F. Williams, Combustion Theory, Benjamin/Cummings, Menlo Park, 2nd edition, 1985.

[80] J. H. Chen, T. Echekki, W. Kollmann, Combust. Flame (1999).

[81] G. Joulin, Combust. Sci. Tech. 97 (1994) 219–229.

[82] J. H. Chen, H. G. Im, Proc. Combust. Inst. 27 (1998) 819–826.

[83] J. Chen, H. Im, Proc. Combust. Inst. 28 (2000) 211–218.

[84] M. Weiß, N. Zarzalis, R. Suntz, Combust. Flame 154 (2008) 671–691.

[85] S. Daniele, J. Mantzaras, P. Jansohn, A. Denisov, K. Boulouchos, J. Fluid Mech. 724 (2013) 36–68.

[86] S. Chaudhuri, F. Wu, C. K. Law, Phys. Rev. E 88 (2013) 033005.

[87] G. Troiani, F. Battista, F. Picano, Combust. Flame 160 (2013) 2029–2037.

[88] K. N. C. Bray, R. S. Cant, Proc. R. Soc. A 434 (1991) 217–240.

[89] D. Bradley, L. A.K.C., M. Lawes, Phil. Trans. Soc. Lond. 338 (1992) 359–387.

[90] P. E. Hamlington, A. Y. Poludnenko, E. S. Oran, Phys. Fluids 23 (2011) 125111.

[91] H. Kobayashi, K. Seyama, H. Hagiwara, Y. Ogami, Proc. Combust. Inst. 30 (2005) 827–834.

[92] T. Y. Hou, Z. Li, S. Osher, H. Zhao, J. Comput. Phys. 134 (1997) 236–252.